AIAA SciTech
13-17 January 2014, National Harbor, Maryland
52nd Aerospace Sciences Meeting

Parametric Study of Boundary-Layer Receptivity to Freestream Hot-Spot Perturbation over a Blunt Compression Cone

Yuet Huang[1] and Xiaolin Zhong[2]
University of California, Los Angeles, California, 90095

This paper presents the numerical simulations of transient flow under the interaction between freestream hotspot perturbations and bow-shock on Purdue's blunt compression cone with the effects of different nose-bluntness and various freestream Mach numbers. The basic flow conditions are referring to Boeing/AFOSR Mach-6 Quiet tunnel (BAM6QT) at Purdue University. The simulations in this paper consist of two cases of different nose-radii and two cases of different freestream Mach numbers. The detailed analysis of the receptivity mechanisms is carried out with linear stability theory (LST). The simulation results agree well with LST analyses. The parametric study is performed by the comparisons of the simulation results with the Mach-6 results that have been carried out previously. The study shows the sharper cone destabilizes the boundary layer, and the higher freestream Mach number stabilizes it. The receptivity mechanisms under both effects are shown to be the same: the second mode instability is induced by the fast acoustic waves behind the shock in the nose region.

Nomenclature

M_∞	=	freestream Mach number
ρ_∞	=	freestream density
T_o	=	total temperature
T_{wall}	=	temperature at the wall
γ	=	ratio of specific heat
Pr	=	Prantl number
R	=	gas constant
μ_r	=	reference viscosity coefficient
T_r	=	reference temperature
T_s	=	Sutherland's temperature
T_∞	=	freestream temperature
e	=	total energy per unit volume
q_j	=	heat flux due to thermal conduction
τ_{ij}	=	shear stress tensor
$\frac{\mathrm{Re}_\infty}{L}$	=	freestream Reynolds number per unit length

I. Introduction

In the development of future hypersonic aerospace vehicles, being able to predict the boundary layer laminar-turbulence transition location on the body surface plays an extremely important role on aerodynamic heating analysis. When the vehicle is travelling in atmosphere at a hypersonic speed, there exist weak disturbances in the freestream and they interact with the boundary layer. The process for the freestream disturbances to cause laminar-turbulence transition can be divided into three stages: (i) boundary layer receptivity, (ii) linear eigenmode growth or transient growth, and (iii) nonlinear breakdown to turbulence [16]. Boundary layer receptivity is the process for the freestream disturbances to enter the boundary layer and generate instability waves. In addition, boundary layer receptivity is a preliminary stage for laminar-turbulence transition to occur [2, 8].

Linear disturbance waves in hypersonic boundary layer contain normal modes. The unstable modes were found by Mack, and he pointed out that the second mode is the dominant instability which leads to transition when Mach number is approximately higher than 4 [7, 19]. During the flight of a hypersonic vehicle, the disturbances in the freestream is weak, thus the boundary layer transition follows the path of normal mode growth of the boundary layer

[1] Post-graduate Student, Mechanical and Aerospace Engineering Department.
[2] Professor, Mechanical and Aerospace Engineering Department, AIAA Associate Fellow.

disturbances and nonlinear breakdown of them. Therefore, the study of second mode receptivity and instability is particularly important.

Most of the hypersonic vehicles have blunt noses in order to reduce aerodynamic heating. The bow-shock in front of the blunt nose creates an entropy layer, which will be swallowed by the boundary layer in downstream [8]. There is strong vorticity created by the entropy layer, which may affect the receptivity process in the flow region near the shock. In addition, the swallowing process of entropy layer has a strong effect on the boundary layer stability [7].

Kovasznay [11] showed that weak disturbances in compressible flow can be decomposed into acoustic, entropy and vorticity disturbance. It is well-known [10] that, regardless of the type of disturbances in the freestream hitting the shock, the interaction with the shock always generates all three kinds of disturbances, namely acoustic, entropy and vorticity disturbances. However, the mechanisms of the interaction of various types of disturbance with the shock are individually different, which would lead to difference in travelling angle and amplitude of the generated disturbances. In nature, the disturbances exist in freestream during flight in atmosphere consist of all three kinds. Thus, detailed boundary layer receptivity studies of all three types of freestream disturbance and shock interaction are necessary for completely understanding the mechanism of hypersonic boundary layer receptivity over blunt body. The receptivity to freestream acoustic disturbances has been studied extensively by many researchers [3, 4]. There is experimental effort at Purdue University to use laser equipments to generate hotspots in a wind tunnel [3, 4]. The goal is to study the generation of the second mode by using freestream entropy perturbations.

The study in this paper is motivated by the experiments at Purdue University. The purpose of the current study is to conduct numerical investigation on the receptivity to hotspot perturbations. The schematic explanation of the laser-spot (hotspot) and cone scenario is demonstrated in Figure 1. The hotspot is generated at a location upstream from the cone on the centerline. Then the spot convects with the hypersonic freestream toward the cone nose, and eventually interacts with and passes through the bow shock, and travels further downstream in shock layer.

Compression cone (see Figure 2) is a circular-base cone with circular-flared geometry along its body in downstream direction. Such geometry was used to enhance the instability under quiet-flow condition due to adverse pressure gradient occurs along the flared geometry of the cone [5, 7].

In Huang & Zhong's [13] hotspot numerical simulation, the results indicate that the freestream entropy perturbation would generate entropy and acoustic disturbances after passing through the bow shock, and the acoustic disturbance behind shock would bounce back from the wall and interact with the bow shock again, and generate acoustic and entropy disturbances.

Ma & Zhong [16] showed that when the acoustic waves generated from freestream entropy perturbation and shock interaction, reaches the boundary layer, the perturbed boundary layer will reflect acoustic waves and transmit to interact with the shock again, and generate additional acoustic, entropy and vorticity disturbances. These additional disturbances combined with the initial disturbances and propagate downstream would produce strong effect on the receptivity. Ma & Zhong have also performed numerical simulation on flat plate with freestream sinusoidal entropy waves at Mach 4.5. They found that the receptivity of supersonic boundary layer to freestream entropy waves is essentially similar to the receptivity to freestream fast acoustic waves; the fast acoustic waves generated behind the shock and propagate downstream into the boundary layer, and excite the instability modes in it. Ma & Zhong has compared their simulation results with McKenzie et al.'s theoretical results, and have good agreement.

Huang & Zhong [38, 39] completed the numerical study of the boundary-layer receptivity mechanism over a blunt compression cone with an entropy spot in Mach-6 freestream. They found that the receptivity mechanism to entropy perturbations is essentially the same as the freestream receptivity to fast acoustic waves, which is consistent to Ma & Zhong's finding [16].

This paper is an extension to the study of the receptivity to an entropy spot in Huang & Zhong [38, 39]. The study has been extended from the receptivity mechanism of a single case to comparisons of mechanisms between different cases with controlled variation in freestream Mach number and nose bluntness.

In the current study, there are two cases under nose bluntness effects and two cases under freestream Mach number effects. The simulations of both the steady base flow and hotspot perturbed transient flow four all the cases are performed. The receptivity mechanisms for all the cases are carried out by comparing the simulation results with the LST analysis. At the end, there are comparisons between all the cases with the previous Mach-6 case in Huang & Zhong [38, 39], and the parametric study is carried out.

II. Governing Equations and Numerical Methods

The governing equations for the numerical simulation of hypersonic perfect-gas flow around compression cone are the following three-dimensional Navier-Stokes equations in conservative-law form and Cartesian coordinates:

$$\frac{\partial U}{\partial t}+\frac{\partial F_j}{\partial x_j}+\frac{\partial F_{vj}}{\partial x_j}=0,\ \ j=1,2,3$$

Vector U contains five conservative-law form dimensional flow variables:

$$U=\begin{bmatrix}\rho & \rho u_1 & \rho u_2 & \rho u_3 & e\end{bmatrix}$$

F_j and F_{vj} are the vectors of convective (invicid) flux and viscous flux in jth spatial direction respectively:

$$F_j=\begin{bmatrix}\rho u_j\\ \rho u_1 u_j+p\delta_{1j}\\ \rho u_2 u_j+p\delta_{2j}\\ \rho u_3 u_j+p\delta_{3j}\\ (e+p)u_j\end{bmatrix}$$

$$F_{vj}=\begin{bmatrix}0\\ -\tau_{1j}\\ -\tau_{2j}\\ -\tau_{3j}\\ -\tau_{jk}u_k-q_j\end{bmatrix},\ k=1,2,3$$

The equation of the state and the transport equations are:

$$p=\rho RT$$

$$e=\rho\left(c_v T+\frac{1}{2}u_k u_k\right)$$

$$\tau_{ij}=\mu\left(\frac{\partial u_i}{\partial x_j}+\frac{\partial u_j}{\partial x_i}\right)-\lambda\frac{\partial u_k}{\partial x_k}\delta_{ij},\ \ \lambda=\frac{2}{3}\mu$$

$$q_j=-\kappa\frac{\partial T}{\partial x_j}$$

where R is the gas constant, C_v is the specific heats that are assumed to be constant with a given specific heat ratio γ. κ is the heat conductivity coefficient, which can be determined with a constant Prantl number. The viscosity coefficient μ is defined by the Sutherland's law:

$$\mu=\mu_r\left(\frac{T}{T_0}\right)^{\frac{3}{2}}\left(\frac{T_r+T_s}{T+T_s}\right)$$

Throughout the numerical methods implementation in the simulation of hypersonic flow around the blunt compression cone, the Cartesian Navier-Stoke's equations have been transformed into body-fitted curvilinear computational domain coordinates (ξ, η, ζ) via Jacobian matrix [6]. The computational domain is bounded by the bow-shock and the wall of the cone, which is called 'shock-fitting' domain. Using shock-fitting method can accurately resolve the position of the bow-shock, which is necessary to obtain the high accuracy of the flow

solutions for receptivity and stability analyses. The shock-fitting grids are moving-grids in time, and the motion is depended on the shock position and the shock velocity. See Figure 3 for a partial view of grid configuration. In each time-step, shock position and shock velocity are the unknowns, and would be solved by the freestream conditions and behind-shock solutions. Spatial discretization of inviscid flux derivatives in stream-wise (ξ) and wall-normal (η) directions are done by using fifth-order finite-difference upwind schemes with local Lax-Friedrichs flux-splitting scheme, and sixth-order central finite-difference scheme is used for viscous flux spatial derivatives. For spatial derivatives in periodic azimuthal direction (ζ), Fourier collocation method has been used. Runge-Kutta method is used for time-marching. The details of shock-fitting method, finite difference schemes and other numerical method implementations of the numerical simulation are explained in Zhong's paper [6].

III. Modeling Equations of Freestream Hotspot Perturbation

Physically a hotspot is an entropy perturbation sphere with acoustic perturbation (weak shock) surrounds it. The entropy core has Gaussian temperature or density distribution [3, 4]. As discussed in Huang & Zhong [13], if the hotspot is relatively large compare to the cone nose, the influence from the acoustic weak shock is very small and negligible. In this case, the hotspot is modeled as a pure entropy perturbation without the acoustic waves. Since the initial position of the hotspot is not far from the shock on centerline in Dunn's paper [1], the time scale for the hotspot to diffuse and propagate in freestream is very small when comparing to the length scale of the initial distance between center of hotspot and shock-front on centerline. Hence, it is reasonable to assume the hotspot profile remains unchanged when convecting with freestream.

For a hotspot model, the perturbed freestream temperature is given by a Gaussian distribution as follows:

$$T = \Delta T_{\max} \exp\left(-\frac{R_c^{\,2}}{2\sigma^2} \right) + T_\infty$$

thus, by ideal gas law, the perturbed freestream density is:

$$\rho = \frac{p_\infty}{R\left(T_{\max} \exp\left(-\frac{R_c^{\,2}}{2\sigma^2} \right) + T_\infty \right)}$$

In a shock-fitting algorithm, it is necessary to determine the time derivative of perturbed freestream density at shock location:

$$\frac{\partial \rho}{\partial \tau} = \left(\frac{p_\infty}{\sigma^2 R} \right) T^{-2} \left(T - T_\infty \right) \left[\left(X_c - U_\infty t \right) \left(\frac{\partial X_c}{\partial \tau} - U_\infty \right) + y_{shk} \frac{\partial y_{shk}}{\partial \tau} + z_{shk} \frac{\partial z_{shk}}{\partial \tau} \right]$$

where σ is Gaussian shaping factor, τ is time in computational domain. X_{spot} is the initial x-coordinate of spot center. The initial x-coordinate difference between the shock location and the spot center is:

$$X_c = \left| X_{spot} - x_{shk} \right|$$

x_{shk}, y_{shk}, z_{shk} are shock-front coordinates. By using the transport equation in mathematics, the distance between hotspot center and any point on the shock front at any time is:

$$R_c = \sqrt{\left(X_c - U_\infty t \right)^2 + y_{shk}^2 + z_{shk}^2}$$

Please note that the time in computational domain is the same as the time in physical domain [6].

IV. Boundary Layer Receptivity Analysis

The hotspot simulation is performed based on the converged mean flow. The temporally varying boundary layer flow variables while the hotspot is passing by the mean flow are recorded at a sufficient temporal well-resolved rate.

However, the recorded boundary layer flow perturbation is a combination of infinite frequency components. In this study, the main interest is to see which frequency would excite instability in boundary layer and how fast is the instability growing spatially. Therefore, it is necessary to have the time-history of the boundary layer perturbation transform into frequency domain, in order to see the behavior of different frequency components. The mathematical method that is used in the instability analysis is Fourier transformation. By definition, continuous Fourier transformation of a flow variable *h(t)* is defined as[20]:

$$H(f) = \int_{-\infty}^{\infty} h(t) e^{2\pi i f t} dt$$

where *h(t)* is the flow variable time function, *H(f)* is its spectral value in frequency domain. Numerically, the continuous Fourier transformed spectral value can be approximated by:

$$H(f_n) \approx \Delta t \sum_{k=0}^{N-1} h_k e^{\frac{2\pi i k n}{N}}$$

where $H(f_n)$ is the spectral value at nth discretized frequency, N is the total number of Fourier collocation points used to discretize the time function, *h(t)*. The discretized time function is h_k. The spectral value, *H(f)*, has real and imaginary components in frequency domain. The $|H(f)|$ is the magnitude of the real part and the imaginary part of *H(f)*. In this paper, *h(t)* is the time-history of boundary layer perturbation, and the *H(f)* is the spectral value of the boundary layer perturbation in frequency domain.

After obtaining the frequency component of the boundary layer, it is necessary to validate the results of the simulation. Here, the comparison with LST is chosen as a method to prove the validity of the simulation. In other papers, such as Zhong [7] and Sivasubramanian [21], the common practice is to compare the local spatial growth rate, local wave number, and the wall-normal boundary layer mode shape with LST.

Local growth rate in linear stability theory (LST) is defined as [19]:

$$\alpha_i = \frac{1}{\left|H(f_n)\right|} \frac{d\left|H(f_n)\right|}{ds}$$

where *s* is the natural coordinate along the body surface. Local wave number in LST is defined as [19]:

$$\alpha_r = \frac{d\varphi_n}{ds}$$

where φ_n is the phase angle of *H(f)* at nth discretized frequency. The wall-normal mode shape is the spatial distribution of the Fourier transformed spectral value, *H(f)*, along the normal of cone surface.

V. Freestream Conditions and Compression Cone Geometries

In order to investigate the effects of nose bluntness and freestream Mach number, there are totally five cases to study. For the nose bluntness effect study, we set up two cases with different nose-radii in addition to the standard case which is simulated by Huang & Zhong [39]. The freestream conditions used in the numerical simulations in this paper is based on Purdue's Mach-6 Quiet Tunnel (BAM6QT) [5]:

$M_\infty = 6.0$
$\rho_\infty = 0.0403\ kg/m^3$
$T_o = 433.0\ K$
$T_{wall} = 300.0\ K$
$\gamma = 1.4$
$Pr = 0.72$
$R = 287.04\ Nm/kgK\ (air)$
$\mu_r = 1.7894 \times 10^{-5}\ kg/ms\ (sea\ level)$
$T_r = 288\ K\ (sea\ level)$

$T_s = 110.3333K$ *(air)*

$\frac{\mathrm{Re}_\infty}{L} = 1.026 \times 10^7 m^{-1}$

The compression cone geometry is based on Schneider's design [5]:

Flare radius = 3.0 *m*
cone half-angle = 2.0 *degrees*
cone length ≈ 0.45 *m*

except that it has two different nose radii:

nose radius = 0.0005 *m* *(Case A1)*
nose radius = 0.0001 *m* *(Case A2)*

in addition to the original nose radius:

nose radius = 0.001 *m* *(Case 0)*

The case with the nose radius of 0.0005 m is named Case A1, and the case with the nose radius of 0.0001 m is named Case A2. The standard case that is completed by Huang & Zhong [39], is named Case 0. It has the original nose radius of 0.001 m.

For the freestream Mach number effect study, we use the original Purdue's geometry:

body-arc radius = 3.0 *m*
cone half-angle = 2.0 *degrees*
cone length ≈ 0.45 *m*
nose radius = 0.001 *m*

In order to have the flow change only under the freestream Mach number effect, we increase the freestream Mach number but keep the freestream unit Reynolds number and the ratio of total temperature in the flow to wall temperature to be the same as the original Purdue's Mach-6 condition, therefore the new Mach-10 flow conditions are:

$M_\infty = 10.0$
$\rho_\infty = 0.01175\ kg/m^3$
$T_o = 432.6\ K$
$T_{wall} = 299.7\ K$
$\gamma = 1.4$
$Pr = 0.72$
$R = 287.04\ Nm/kgK$ *(air)*
$\mu_r = 1.7894 \times 10^{-5}\ kg/ms$ *(sea level)*
$T_r = 288\ K$ *(sea level)*
$T_s = 110.3333K$ *(air)*
$\frac{\mathrm{Re}_\infty}{L} = 1.026 \times 10^7 m^{-1}$

The case with Mach-10 flow conditions is named Case B1. Furthermore, the new case of Mach-15 flow conditions is named Case B2. The flow conditions are:

$M_\infty = 15.0$
$\rho_\infty = 0.00764\ kg/m^3$
$T_o = 920\ K$
$T_{wall} = 637.4\ K$
$\gamma = 1.4$
$Pr = 0.72$

R = 287.04 *Nm/kgK (air)*
μ_r = 1.7894 x 10^{-5} *kg/ms (sea level)*
T_r = 288 *K (sea level)*
T_s = 110.3333*K (air)*
$\frac{\mathrm{Re}_\infty}{L} = 1.026 \times 10^7 m^{-1}$

The standard case is Case 0 that is the same as the standard case for studying the effect of nose bluntness.

VI. Freestream Hotspot Parameters

The peak radius is controlled by the Gaussian factor, σ. The hotspot size is referred to the actual hotspot size in Purdue's experiments [3, 4], which is case A in Huang & Zhong [13]. The initial location of the hotspot is chosen to be 2 cm upstream to the origin of the coordinates along the x-coordinate.

σ = 0.001 (largest radius: r = 0.003 m), X_{spot} = -0.02 m

In order to keep the disturbance linear in the flow, the maximum temperature perturbation amplitude is chosen to be:

$$\Delta T_{\max} = T_\infty \times 10^{-4}.$$

The profiles of the freestream temperature and density distribution in radial-direction within a modeled 3D hotspot under the Mach-6 flow conditions are demonstrated in Figure 4 and Figure 5.

VII. Results

All flow variables shown in the figures are dimensionless, which are normalized by the corresponding freestream values. For all contour plots, the upper boundary is the location of the shock, the lower boundary is the cone-wall, the left boundary is the flow inlet, and the right boundary is the flow exit. Since the cone is at zero degree angle of attack, only the upper half of the cone is demonstrated, and the lower half is the mirror image of the upper half due to axis-symmetry of the flow. Figure 3 shows the partial view of the computational grid structure around the cone. Due to the limiting computer power for computing almost a million grid points at once, the simulation is divided into 18 zones. Zone 1 is the computation domain that wraps around the hemispherical cone nose, zone 2 to zone 18 wrap around the compression wall of the cone.

There are five parametric cases to be investigated, which are summarized in the following table:

Case Name	Nose Radius	Freestream Mach Number
0	0.001 m	6
A1	0.0005 m	6
A2	0.0001 m	6
B1	0.001 m	10
B2	0.001 m	15

Table 1. Summary of Case Parameters

There are two directions for the current parametric study. One of them is the nose bluntness effects, and the other one is the freestream Mach number effects.

1. Nose Bluntness Effects

A. Evolution of the Boundary-Layer Disturbances

The spatial developments of pressure perturbations at wall for of Case 0, A1 and A2 are demonstrated in Figure 6 to Figure 11. The magnitudes of the perturbations are normalized by the freestream pressure. The time-history profile of the perturbations for Case 0 begins from a location, x=0.0135 m, not far behind the nose region. The shape at this location is relatively monotonic. While the perturbations moving downstream in the upstream region, the amplitude decays and the profile gradually become more complicated and spread-out. At the beginning location in the downstream region, the profile split into two waveforms in time: one is more oscillatory followed by a smoother profile. Both parts become further apart from each other, since the more oscillatory waves travel faster than the

smoother waves. Their amplitudes decay while the perturbations travel downstream before reaching x=0.25 m. At x=0.25m, there is a new waveform appears behind the smoother waves. The amplitude of this new waveform grows rapidly. The amplitude of the new waveform soon surpasses the amplitudes of the decaying waves and dominates the entire perturbations.

The time-history profiles of the perturbations for Case A1 and A2 are plotted at various streamwise locations from the nose region to the downstream region of the cone in Figure 8 to Figure 11. For Case A1 that is shown in Figure 8, the profile begins with a Gaussian shape in the nose region. This Gaussian shaped profile is directly related to the Gaussian freestream perturbations that enter the shock layer in the nose region. Two different waveforms, an oscillatory one followed by a single peaked one, appear in the profile behind x=0.08 m in the upstream region. The amplitude decays in the upstream region. In the downstream region shown in Figure 9, the single peaked waves become oscillatory, and their amplitude grows. The shapes throughout the evolution of the perturbations for Case A1 are similar to Case 0.

For Case A2, the profile initially has a Gaussian shape in the nose region. While the perturbations moving downstream in the upstream region, their profile gradually becomes multi-peaked, and their overall amplitude decays. Such trend is revealed in Figure 10. After the perturbations entering the downstream region at x=0.054 m, which is shown in Figure 11, the shape becomes more oscillatory, and the overall amplitude increases. The evolution of the profile is caused by the evolution of eigenmodes in the boundary layer disturbances, which is presented in the latter section.

From the above observations, the overall patterns of disturbances evolution in boundary layer are consistent for all three cases of bluntness effects. They all begins from a monotonic profile, and gradually become multi-peaked. The amplitudes decay while moving downstream in upstream region. After their entrance to downstream region, an oscillatory and dominant growing waveform appears behind the original decaying waves.

One can calculate the average speeds of the disturbances by dividing the travelled distance of the disturbances with the time elapsed from Figure 6 to Figure 11. The average speed of the wave front of Case A1 behind the nose region is around 1006 m/s. The average speed of the wave front behind the nose region is around 1009 m/s for Case A2. The average speed of the wave front in Case 0 behind the nose region is around 1008 m/s. Therefore, we can see that the average speeds of the wave front for the cases of bluntness effects are approximately the same.

In Figure 11, the amplitude growth of the perturbations appears from 0.054 m to 0.102 m for Case A2. The amplitudes of perturbations within this spatial range are still decaying before reaching the unstable region in Case 0 and A1. Similarly, the amplitude growth of the perturbations appears from 0.17 m to 0.215 m in Case A1. The amplitudes of perturbations within this spatial range are still decaying before reaching the unstable region in Case 0. Therefore, the amplitude comparisons cannot be conducted at the current stage. Both Case A1 and A2 need to be simulated further downstream in order to compare the amplitude growth with Case 0.

However, at the current stage, the approximate location of growth can be obtained and compared. For Case 0, the growth begins around x=0.25 m. For Case A1, the growth begins around x=0.17 m, and the location for Case A2 is x=0.054 m. By comparing these results, we can see that the smaller nose radius cone has the earlier growing location of boundary layer disturbances.

B. Spectra of the Boundary-Layer Disturbances

In order to investigate the spectral characterization of the boundary layer disturbances, we transform the time-history traces into frequency domain, and the spectra of the wall pressure perturbations are obtained. The spectra of the normalized wall pressure perturbation at various locations throughout the cone for Case 0, A1 and A2 are shown in Figure 12 to Figure 14.

In Case 0, Figure 12, there is a growing peak appears between 260 kHz to 320 kHz, which is the unstable frequency range, from x=0.21 m to 0.394 m. The bandwidth of the unstable frequency is 60 kHz. The frequency shift of the growing peak is very minimal. The peak frequency is consistently around 290 kHz due to the flaring of the cone is designed to create a constant boundary layer thickness downstream along the cone with 1 mm nose radius under the Mach 6 flow conditions. The oscillation in the spectra is caused by the modulation of multi-mode waves, when there is no dominant wave.

In Case A1, Figure 13, the growing peak shifts from 343 kHz to 319 kHz between x=0.125 m to 0.232 m. The compression cone design can no longer create a boundary layer with the constant thickness. The unstable frequency range at the last plotted location is from 260 kHz to 362 kHz, hence the bandwidth of the unstable range is 102 kHz.

In Case A2, Figure 14, the growing peak shifts from 518 kHz to 402 kHz between x=0.054 m to 0.115 m. The compression cone design can no longer create a boundary layer with the constant thickness. The unstable frequency range at the last location plotted is from 240 kHz to 440 kHz, hence the bandwidth of the unstable range is 200 kHz.

The peak frequency down-shifts of the 0.1 mm and 0.5 mm radii cases are caused by increase of boundary layer thickness in streamwise direction. Therefore, the smaller nose radius would lead to increase in the boundary layer thickness downstream. Also by comparing the bandwidths of Case 0, A1 and A2, one can see that the smaller radius cone has the wider unstable frequency bandwidth. The peak frequency between Case A1 and A2 is not valid for comparison, since the amplification locations of Case A1 do not overlap the one of Case A2. However, it is obvious that the peak frequency of Case 0 is lower than Case A1 at x=0.232 m. Therefore, it is likely that the cone with the smaller radius has the higher peak frequency.

The amplification of the disturbances is different for each case, since it is depended on the specific geometry and flow conditions. At x=0.13 m of Case 0, the maximum normalized amplitude within the unstable range is 0.0117. At x=0.125 m of Case A1, the maximum normalized amplitude within the unstable range is 0.0279. At x=0.115 m of Case A2, the maximum normalized amplitude within the unstable range is 1.52. This shows the smaller the nose radius is, the more amplification of the boundary layer disturbances is.

C. Boundary Layer Receptivity Analysis

LST analyses based on the steady base flow are conducted in order to identify the modal behavior in the linear regime. We choose a sampling frequency that is very close to the peak frequency at the most downstream location in the simulated disturbance spectra, to perform the spatial comparisons between the numerical simulated results and those from LST. In Case 0, the peak frequency of 293 kHz is selected. In Case A1, the peak frequency of 337 kHz at x=0.364 m is chosen. In Case A2, the peak frequency of 557 kHz is selected. However, 557 kHz in Case A2 is the one that is very close to the peak frequency at x=0.054 m. This was the most downstream location at the time of initial stage of the study. Therefore, we will conduct further analyses with the updated sampling frequencies.

In order to identify the modal evolution during the receptivity process, the simulated phase speeds are compared with the LST ones. In Figure 15 to Figure 17, the comparisons of non-dimensional streamwise phase speeds between the simulations and LST of Case 0, A1 and A2 are shown. In Case 0, Figure 15, before reaching s=0.04 m, the simulated disturbance phase speeds is very close to the phase speed of the mode F which is initially excited by the fast acoustic waves in the nose region. Then the simulated phase speed become very oscillatory between s=0.04 m to s=0.2 m. The oscillation is caused by the multi-mode wave modulation where there is no dominant mode in the boundary layer. Behind the phase speeds synchronization location of the mode S and F at s=0.16 m, the simulated phase speeds converge to the one of mode S. The oscillation also attenuates rapidly. These observations show that the boundary layer disturbances are most likely to be excited by the fast acoustic waves that are generated by the shock/entropy spot interaction in the nose region. The boundary layer disturbances contain relatively strong mode F before they reach the modulation region. Then the boundary layer disturbances become dominated by the mode S behind the synchronization region.

The evolution of phase speeds for both Case A1 and A2 are similar. The simulated phase speeds are close to the mode F in the upstream region. Then the simulated phase speeds switch to match the mode S behind the synchronization region. From Figure 16 and Figure 17, one can see the mode S/F synchronization region of Case A1 and A2 are around 0.118 m and s=0.04 m respectively. Hence, the smaller nose radius would likely leads to an earlier synchronization region. The discontinuity of the mode F curve indicates that there are multiple modes exist very close to the mode F when crossing the continuous spectrum. The oscillatory curves indicate that the multi-mode modulations appear in the boundary layer disturbances. The oscillation in the simulated phase speeds attenuate and converge to mode S behind the synchronization region indicates that the boundary layer disturbances become dominated by mode S. Therefore, the receptivity mechanism of Case A1 and A2 are the same to Case 0. They are initially excited by the fast acoustic waves in the nose region, and then they have relatively strong mode F in the upstream region. The synchronization of mode S/F causes the disturbances to be dominated by the mode S.

The comparison of the negative growth rates between the simulated disturbances and LST for Case 0, A1 and A2 are shown in Figure 18 to Figure 20. The Branch-I neutral point of boundary layer instabilities for Case A1 and A2 are s= 0.0715 m and 0.0284 m. The one for Case 0 is s=0.11 m. By comparing both phase speed and growth rate results, the Branch-I neutral point appears in the earlier part of the synchronization region for the Mach 6 cases with variations in nose radius. The simulated growth rates converge to the mode S downstream, and it becomes unstable which is indicated by having the negative growth rates less than zero. The simulated growth rates appear to be less than the mode F ones. It is possibly due to the surface curvature and non-parallel effects are not considered in the current LST model. In Case A1, the negative growth rate of mode S at s=0.127 m is -41.7 m^{-1}. The negative growth rate of mode S at s=0.0372 m is -27.2 m^{-1} for Case A2. In Case 0, the negative growth rate of mode S at s=0.127 is -13.6 m^{-1}. From the above growth rate study, the smaller nose radius would likely lead to an earlier Branch-I neutral point location, and higher growth rates.

2. Freestream Mach Number Effects

A. Evolution of the Boundary-Layer Disturbances

The spatial developments of pressure perturbations at wall for Case B1 and B2 are demonstrated in Figure 21 and Figure 22. The magnitudes of the perturbations are normalized by the freestream pressure. The time-history profiles of the perturbations are plotted at various streamwise locations from the nose to the downstream region of the cone. Case B1 and B2 are plotted at the same streamwise locations.

The perturbations of both Case B1and B2 have a Gaussian profile in the nose region at x=-0.001 m. This Gaussian shaped profile is directly related to the Gaussian freestream perturbations that enter the shock layer in the nose region. The shape becomes multi-peaked while moving downstream in the upstream region between x=0.011 m to 0.07 m. The growth begins at the first location of x=0.07 m in the downstream region. Behind x=0.16 m, the rear part of the profile becomes very oscillatory and its amplitude grows rapidly and dominantly. By comparing both Case B1 and B2, the overall amplitude of Case B1 is less than the one of Case B2. Eventually, they become the same order of magnitude at the location, x=0.34 m, near the end of the cone.

The average decay rate can be calculated by dividing the difference in the maximum normalized magnitude by the distance travelled. The average decay rate of the amplitude for Case B1 is approximately 0.197 m^{-1} in the upstream region. The average decay rate for Case B2 is approximately 0.422 m^{-1} in the upstream region. The average rate of growth in the downstream region for Case B1 is around 0.00217 m^{-1}. The one for Case B2 is 0.00208 m^{-1}. Hence, the amplitude of Case B2 decays faster than Case B1 in the upstream region. The amplitude of Case B2 grows slightly slower than Case B1.

One can calculate the average speeds of the disturbances by dividing the travelled distance of the disturbances with the time elapsed from Figure 21 and Figure 22. The average speeds of wave front behind the nose region for Case B1 and B2 are 866 m/s and 1320 m/s. The average speed of wave front behind the nose region for Case 0 is 1008 m/s. Hence, there is no clear trend to relate the wave front speed with the freestream Mach number.

B. Spectra of the Boundary-Layer Disturbances

In order to investigate the spectral characterization of the boundary layer disturbances, we transform the time-history traces into frequency domain, and the spectra of the wall pressure perturbations are obtained. The spectra of the wall pressure perturbation at various spatial locations from nose to downstream regions for Case B1 and B2 are shown in Figure 23 and Figure 24. In Case B1, the growing peak shifts from 108 kHz to 124 kHz between x=0.16 m to 0.364 m. The unstable frequency range at the last plotted location is from 20 kHz to 196 kHz, thus the bandwidth of the unstable range is 176 kHz. In Case B2, the growing peak shifts from 83 kHz to 126 kHz between x=0.1 m to 0.364 m. The unstable frequency range at the last plotted location is from 19 kHz to 548 kHz, thus, the bandwidth is 529 kHz. In Case 0, Figure 12, the peak frequency shift is very minimal, and the bandwidth is 60 kHz.

The up-shifts of peak frequencies for Case B1 and B2 are due to the thinning of the boundary layer downstream. Therefore, having a higher freestream Mach number would lead to decrease in the boundary layer thickness downstream. From the bandwidth comparison, one that concludes that having a higher freestream Mach number would results a wider unstable frequency bandwidth. However, there is no clear trend to show the higher freestream Mach number would results in a lower peak frequency downstream, which is due to the stronger compression effects.

In Case 0, Figure 12, the maximum normalized amplitude at x=0.354 m and 0.374 m are 15.6 and 52.3 respectively. The maximum normalized amplitude at x=0.364 m is 104 for Case B1, and the one for Case B2 is 45.7. The results of different Mach number cases do not show a trend between the amplitude and the freestream Mach number.

C. Boundary Layer Receptivity Analysis

LST analyses based on the steady base flow are conducted in order to identify the modal behavior in the linear regime. We choose a sampling frequency that is very close to the peak frequency at the most downstream location in the simulated disturbance spectra, to perform the spatial comparisons between the numerical simulated results and those from LST. For both Case B1 and B2, we have chosen the frequency of 130 kHz. For Case 0, the frequency of 293 kHz is selected.

The comparisons of non-dimensional streamwise phase speeds between the simulations and LST for Case B1 and B2 are shown in Figure 25 and Figure 26. Similar to the receptivity mechanism of Case 0, which is revealed in the phase speed plot of Case 0 in Figure 15, the boundary layer disturbances in Case B1 and B2 are most likely to be excited by the fast acoustic waves, which are generated by the shock/entropy spot interaction in the nose region. The boundary layer disturbances contain relatively strong mode F before they reach the mode S/F synchronization region. The mode S/F synchronization region of Case B1 is around s=0.08 m. The synchronization region for Case

B2 is approximately around s= 0.073 m. The one from Case 0 is s=0.16 m. Hence, the higher freestream Mach number would likely leads to the earlier synchronization region.

The discontinuity of the mode F curve indicates that there are multiple modes exist very close to the mode F when crossing the continuous spectrum. The oscillatory curves indicate the multi-mode modulations appear in the boundary layer disturbances. The oscillation in the simulated phase speeds attenuate and converge to mode S behind the synchronization region indicates that the boundary layer disturbances become dominated by mode S.

The comparison of the negative growth rates between the simulated disturbances and LST in Case B1 and B2 are shown in Figure 27 and Figure 28. The Branch-I neutral point of boundary layer instabilities for Case B1 and B2 are s=0.09 m and 0.145 m. In Figure 18, the Branch-I neutral point for Case 0 is s=0.11 m. By comparing both phase speed and growth rate results, the Branch-I neutral point appears in the later part of the synchronization region for the higher Mach number cases. The simulated growth rates converges to the mode S downstream, and it becomes unstable which is indicated by having the negative growth rates less than zero. The simulated growth rates appear to be less than the mode F ones. It is possibly due to the surface curvature and non-parallel effects are not considered in the current LST model. In Case B1 and B2, the negative growth rates of mode S at s=0.283 m are -23.6 m^{-1} and -8.86 m^{-1} respectively. In Case 0, Figure 18, the negative growth rate of mode S at s=0.283 m is -47.1 m^{-1}. From the above growth rate study, the higher freestream Mach number case would tend to have lower growth rates, but there is no trend shown to relate the Branch I neutral point with the freestream Mach number.

VIII. Conclusions

In the current, we have simulated the freestream hotspot perturbed transient flow under two types of effects: the effects of nose bluntness and the effects of freestream Mach number. The simulations are well agreed with the LST analyses. The receptivity mechanisms are identified by comparing the simulated results with the LST analyses. After comparing all the results from the cases within each effect, and comparing the results with the previously obtained standard case, the parametric study is eventually carried out.

By comparing the results in this paper to those of previously completed standard Mach 6 freestream case with the nose radius of 1 mm case, one can see the following trends for the compression cone:

(i) The smaller nose radius would lead to increasing the boundary layer thickness downstream.
(ii) The smaller nose radius would lead to a wider unstable second mode frequency bandwidth.
(iii) Having a higher freestream Mach number would lead to decrease in the boundary layer thickness downstream.
(iv) The higher freestream Mach number would also lead to a wider unstable second mode frequency bandwidth.
(v) The cone with the smaller radius is likely to have the higher peak frequency.
(vi) The smaller nose radius cone has higher second mode amplitudes of the boundary layer disturbances.
(vii) The receptivity mechanisms of all four cases are similar to the standard case; the boundary layer disturbances are most likely to be excited by the fast acoustic waves that are generated by the shock/entropy spot interaction in the nose region. In the upstream region, the boundary layer disturbances have relatively strong mode F before they reach the mode S/F synchronization region. Behind the synchronization region, the disturbances become unstable and dominated by mode S, which is the unstable second mode.
(viii) The cone with a smaller nose radius is likely to have an earlier synchronization region.
(ix) Having a higher freestream Mach number would also leads to an earlier synchronization region.
(x) The cone with a smaller nose radius is likely to have the Branch-I neutral point appears earlier.
(xi) The sharper cone is likely to have higher second mode growth rates.
(xii) Having a higher freestream Mach number, the second mode growth rates become lower.

Therefore, in a hypersonic freestream, a sharper cone nose destabilizes the boundary layer under the effect of freestream entropy perturbations, and the higher freestream Mach number stabilizes the boundary layer.

In order to provide a clearer picture of the parametric study, the case of 0.1 mm needs to be updated with the latest peak frequency. Both 0.1 mm and 0.5 mm case need to compute further downstream and to be compared with the standard case.

Appendix

All flow variables shown in the figures are dimensionless, which are normalized by the corresponding freestream values.

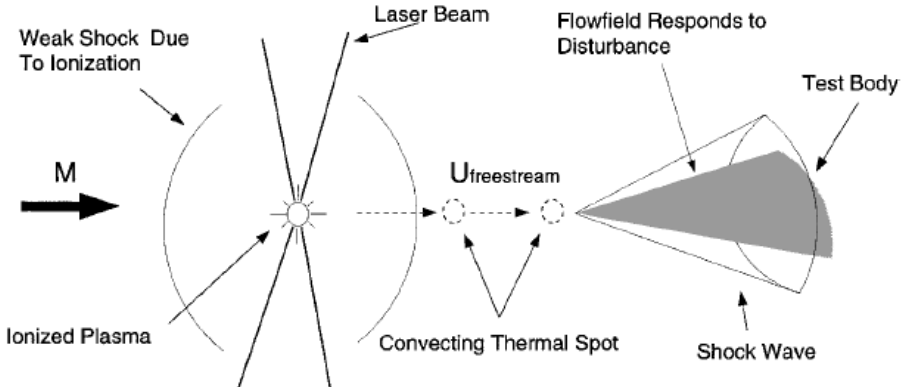

Figure 1. Schematic explanation of the laser-spot and cone scenario. [9]

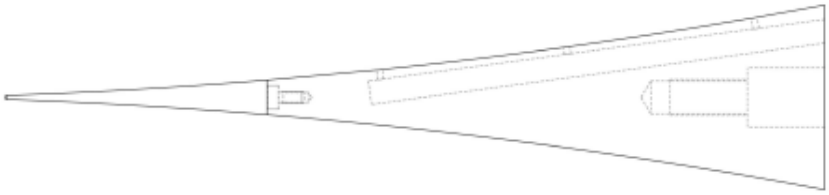

Figure 2. Schematic diagram of Purdue's Compression Cone [5]

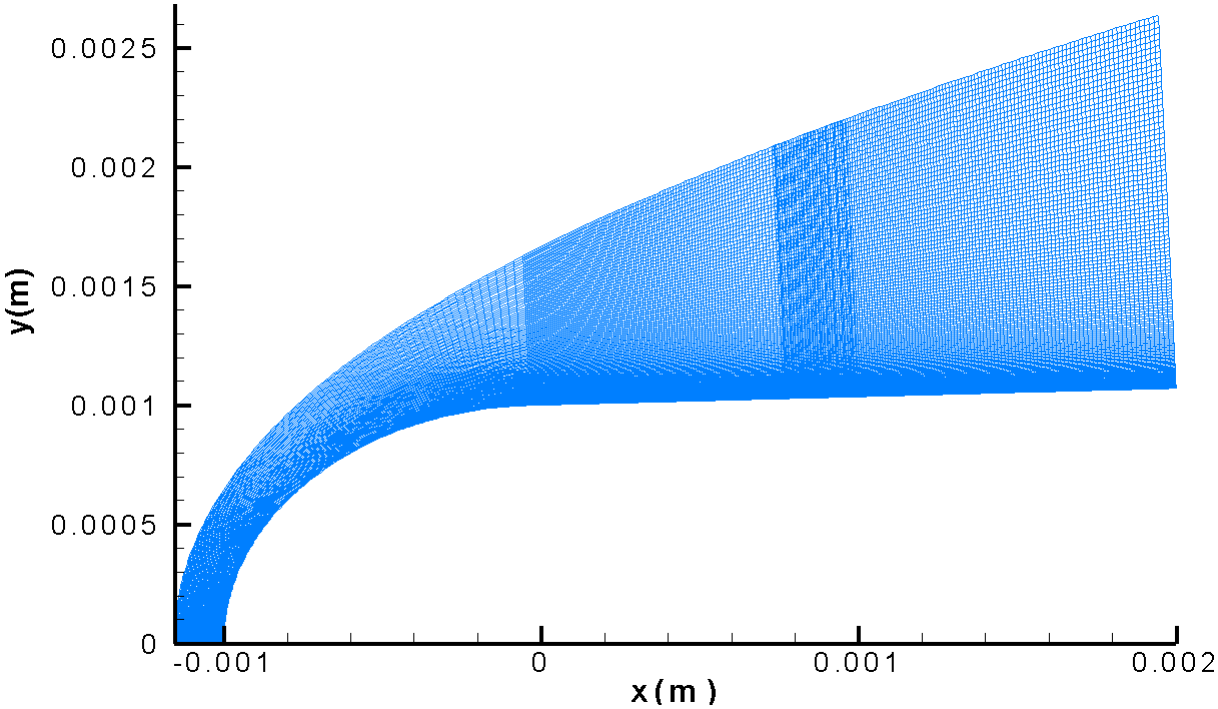

Figure 3. Partial view of grid configuration in zone 1, 2 and 3.

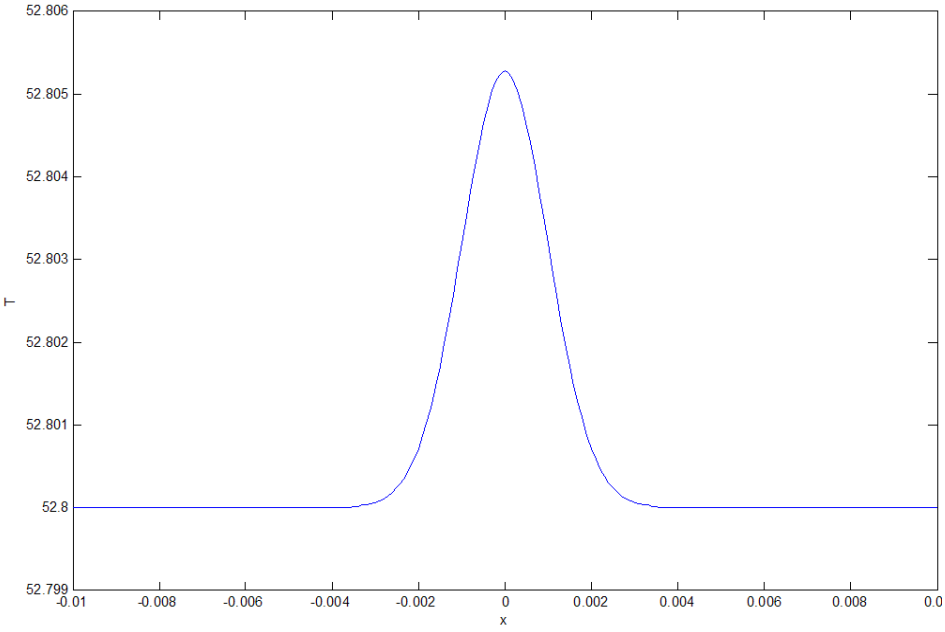

Note: x is radius in meter, T is temperature in degree Kelvin.

Figure 4. Gaussian distribution of perturbed temperature in radial-direction.

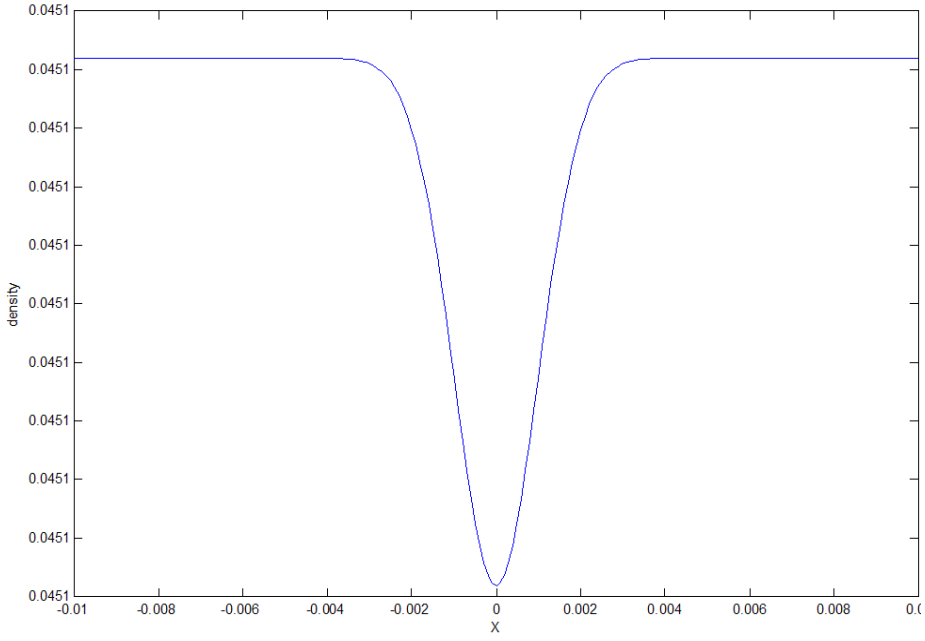

Note: x is radius in meter, density is in kg/m^3.

Figure 5. Gaussian distribution of perturbed density in radial-direction.

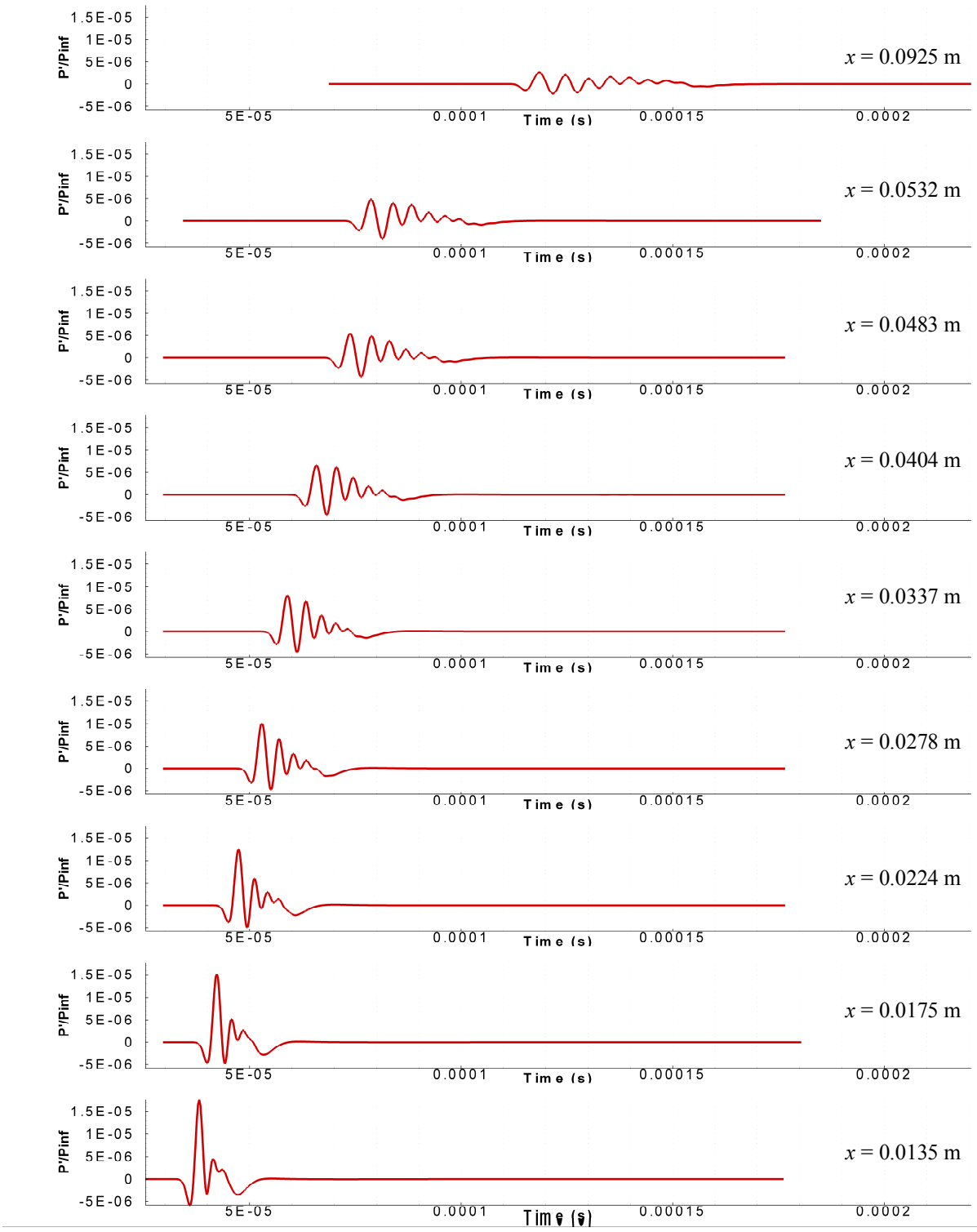

Figure 6. Time-history traces of pressure wall-perturbations at various streamwise locations in upstream region of the cone for Case 0.

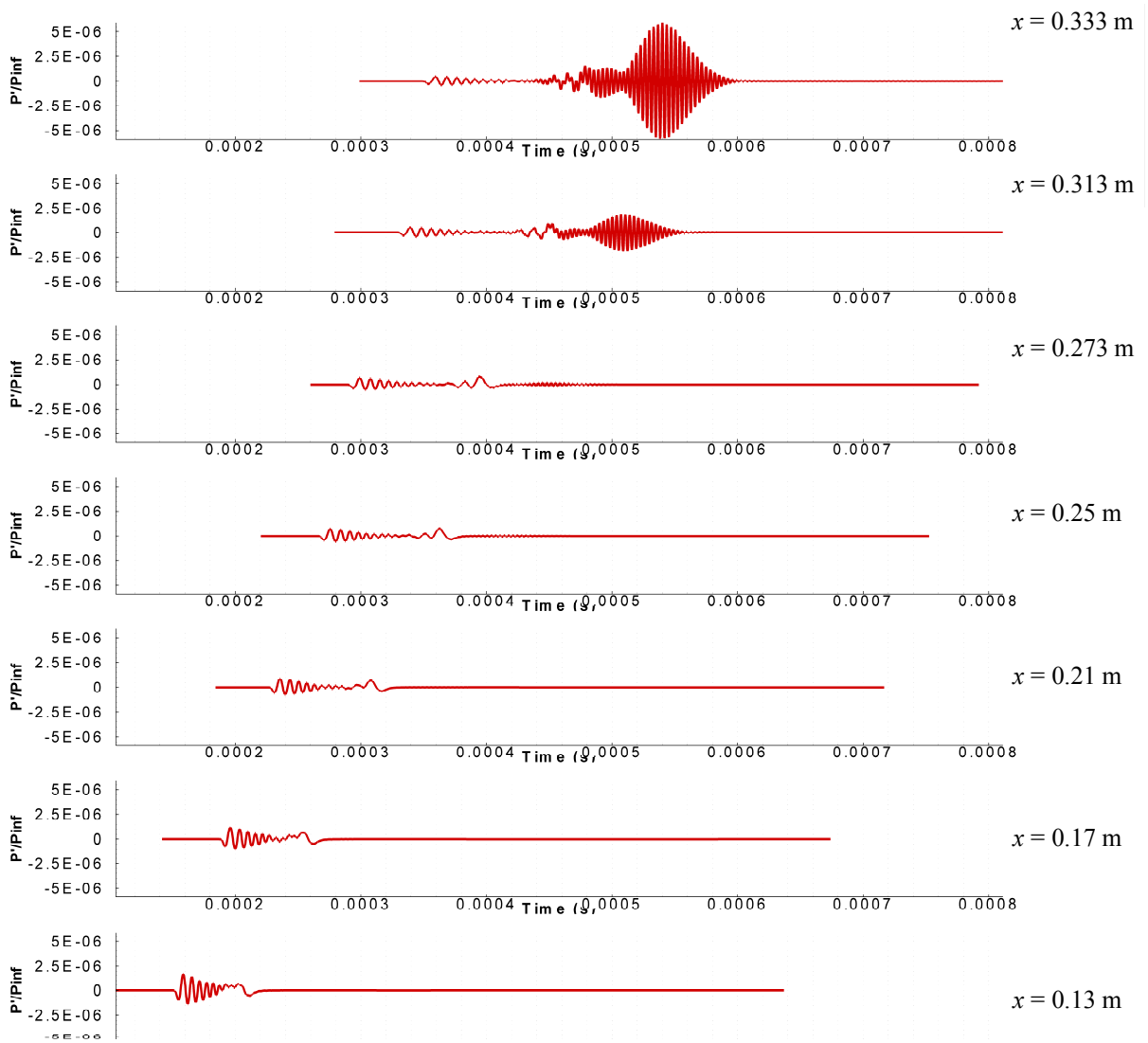

Figure 7. Time-history traces of pressure wall-perturbations at various streamwise locations in downstream region of the cone for Case 0.

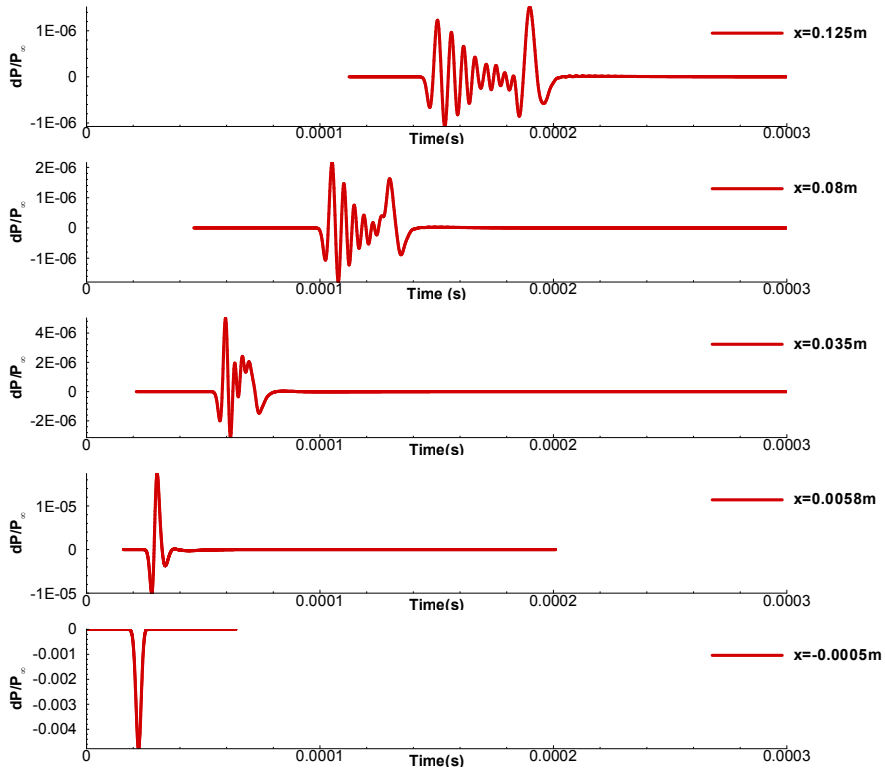

Figure 8. Time-history traces of pressure perturbations at wall at various streamwise locations over the upstream regions of the cone for Case A1.

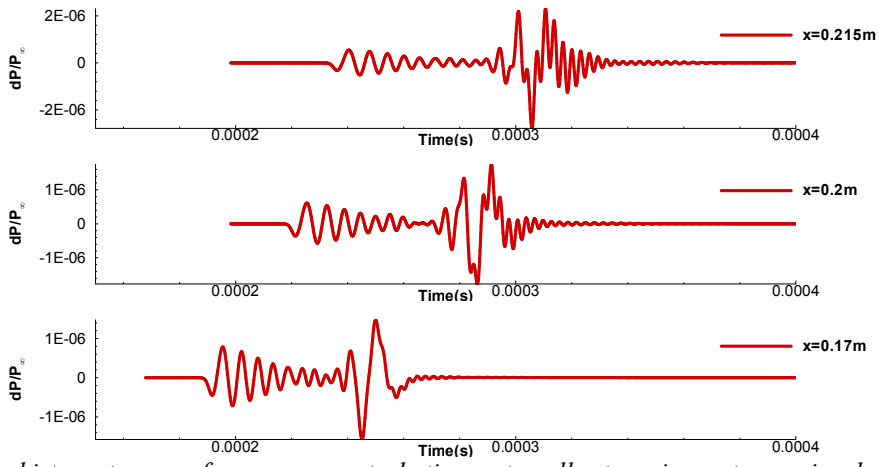

Figure 9. Time-history traces of pressure perturbations at wall at various streamwise locations over the downstream regions of the cone for Case A1.

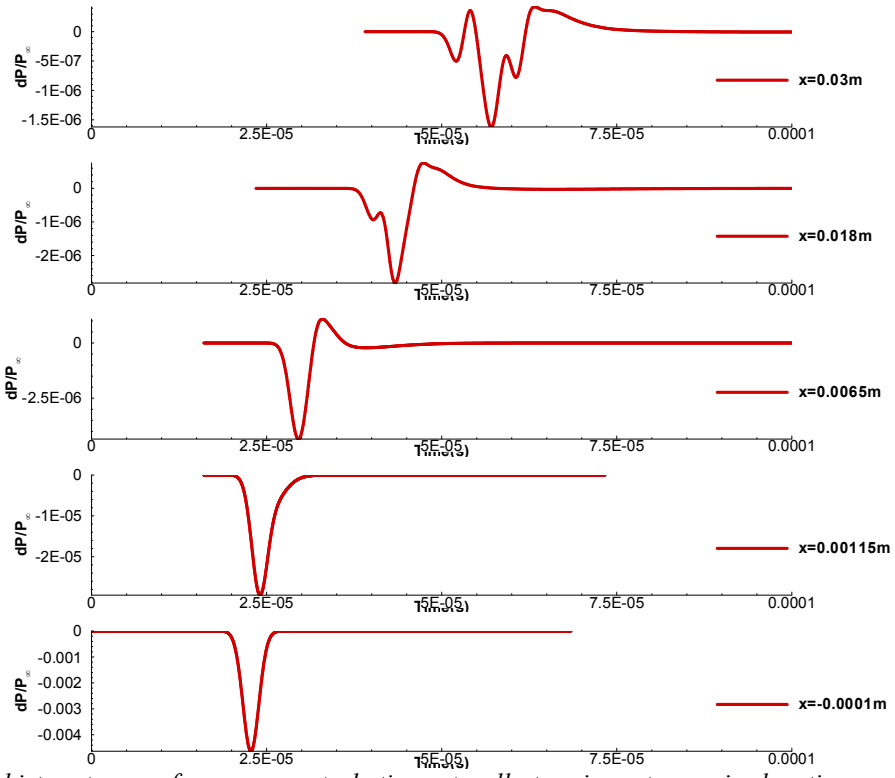

Figure 10. Time-history traces of pressure perturbations at wall at various streamwise locations over the upstream regions of the cone for Case A2.

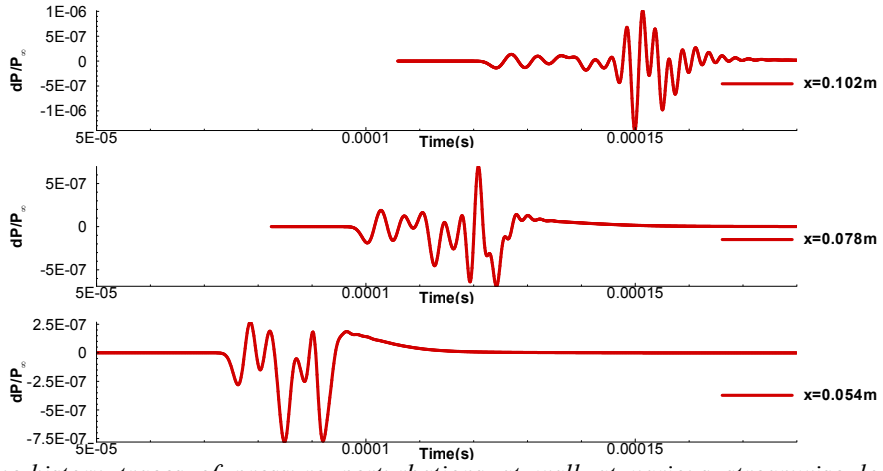

Figure 11. Time-history traces of pressure perturbations at wall at various streamwise locations over the downstream regions of the cone for Case A2.

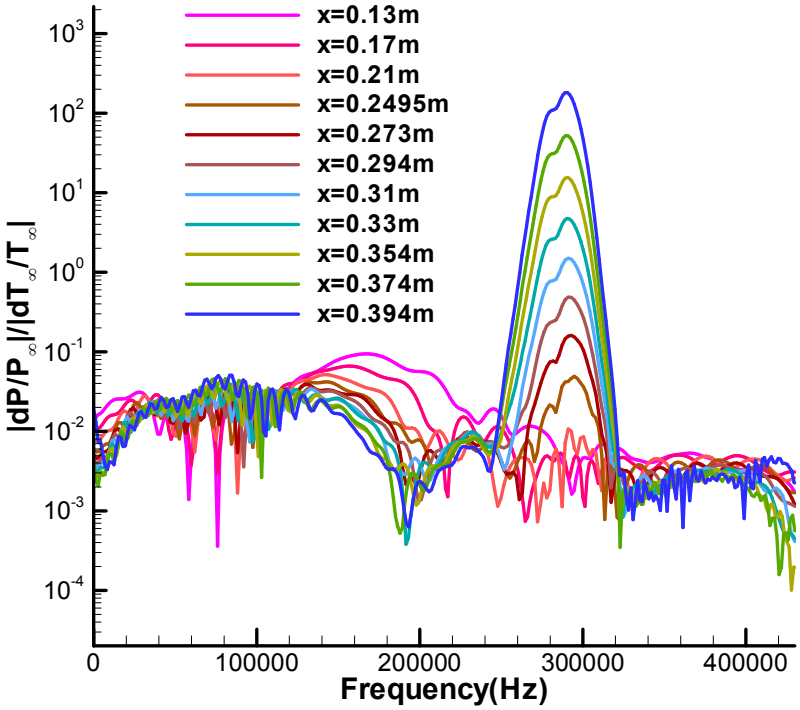

Figure 12. Non-dimensional frequency spectrum of pressure perturbations at wall relative to freestream perturbations at various location over the cone for Case 0.

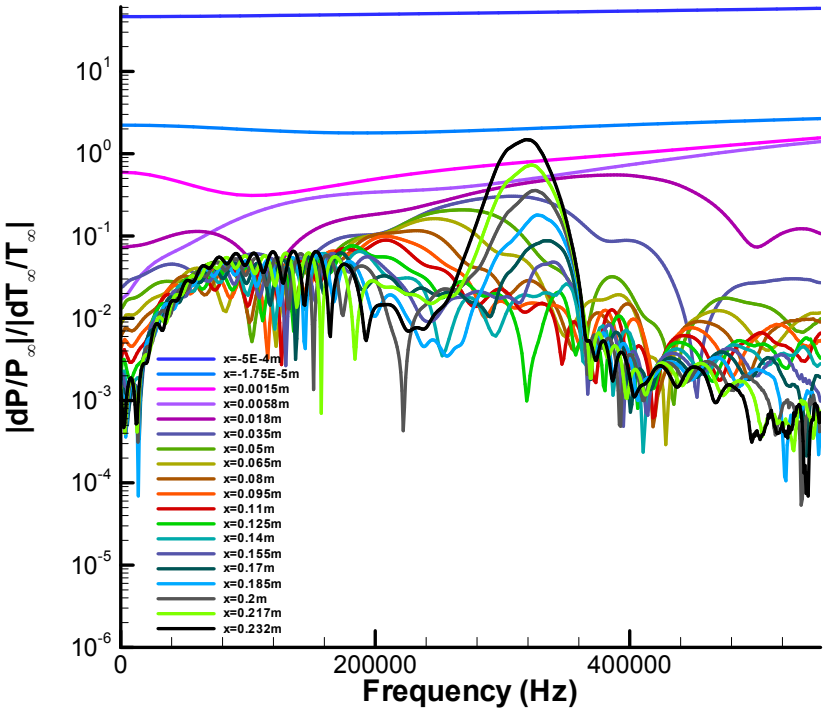

Figure 13. Non-dimensional frequency spectrum of pressure perturbations at wall relative to freestream perturbations at various location over the cone for Case A1.

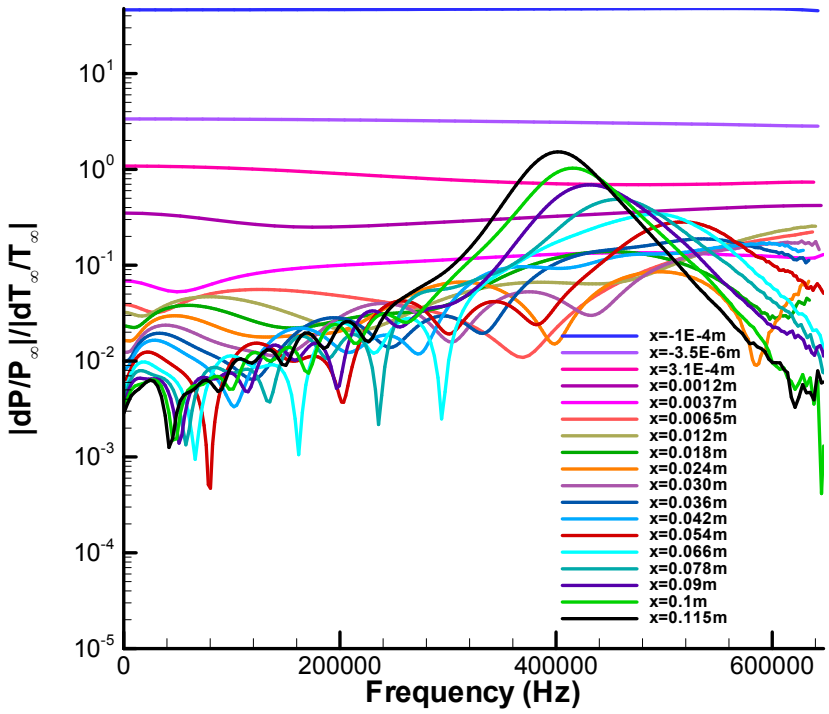

Figure 14. Non-dimensional frequency spectrum of pressure perturbations at wall relative to freestream perturbations at various location over the cone for Case A2.

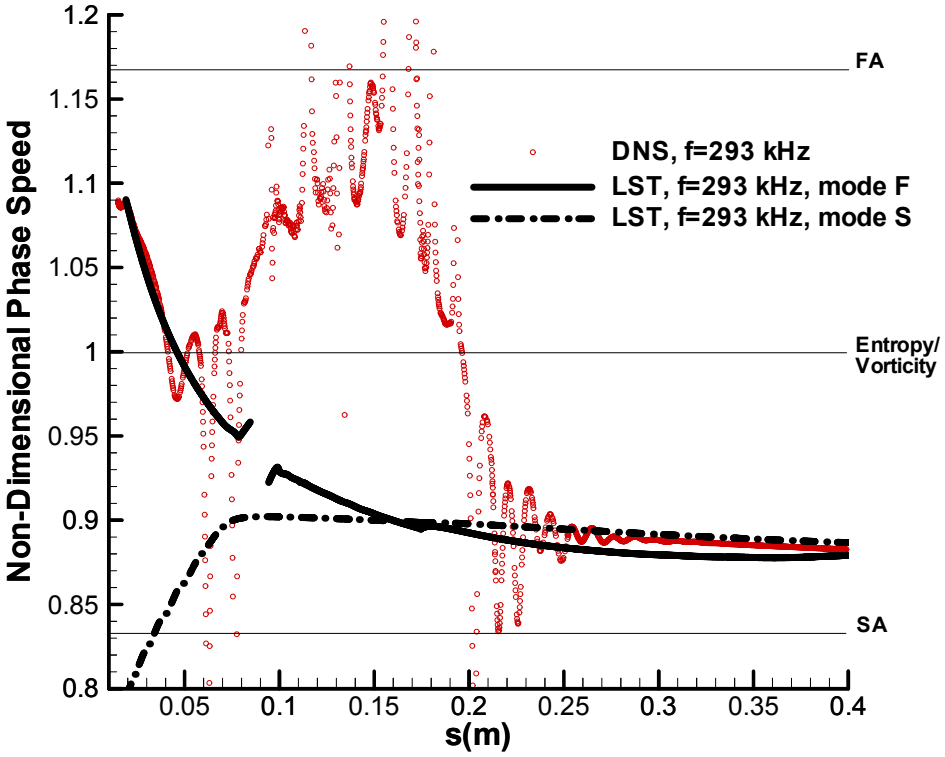

Figure 15. Comparison of the streamwise phase speeds of the simulated wall disturbances with those of mode F and S by LST for Case 0.

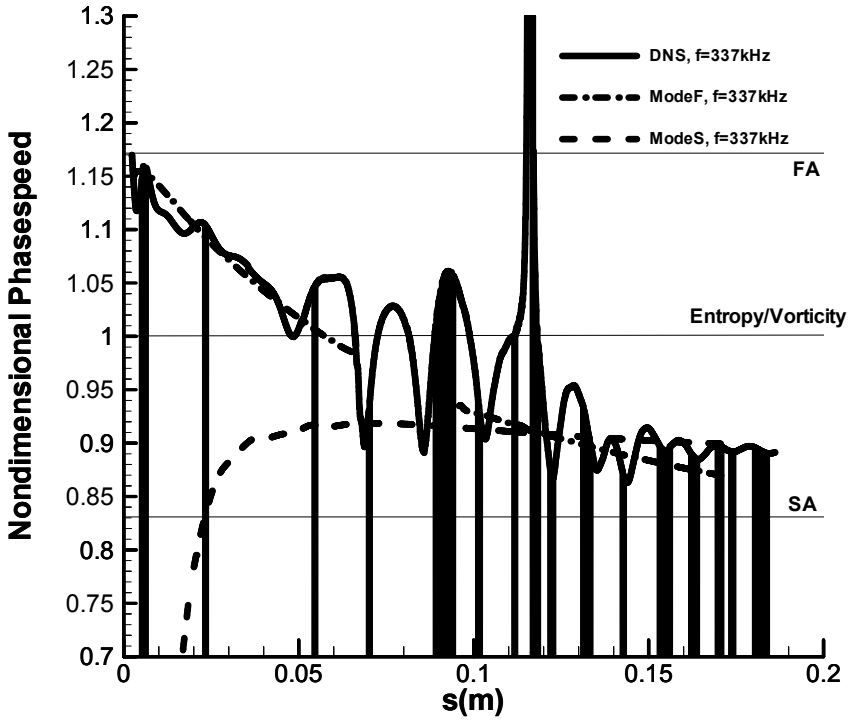

Figure 16. Comparison of the streamwise phase speeds of the simulated wall disturbances with those of mode F and S by LST for Case A1.

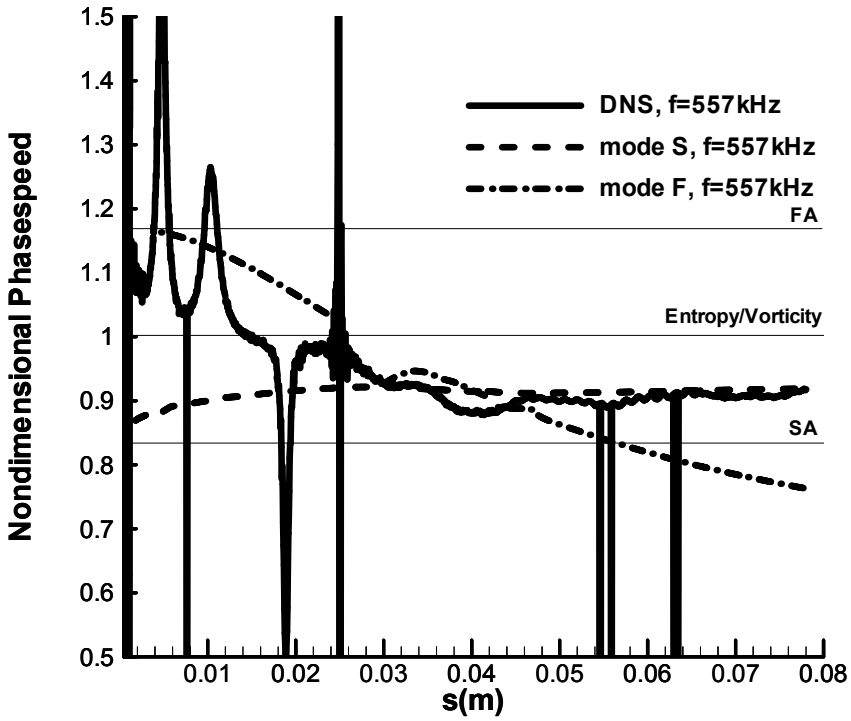

Figure 17. Comparison of the streamwise phase speeds of the simulated wall disturbances with those of mode F and S by LST for Case A2.

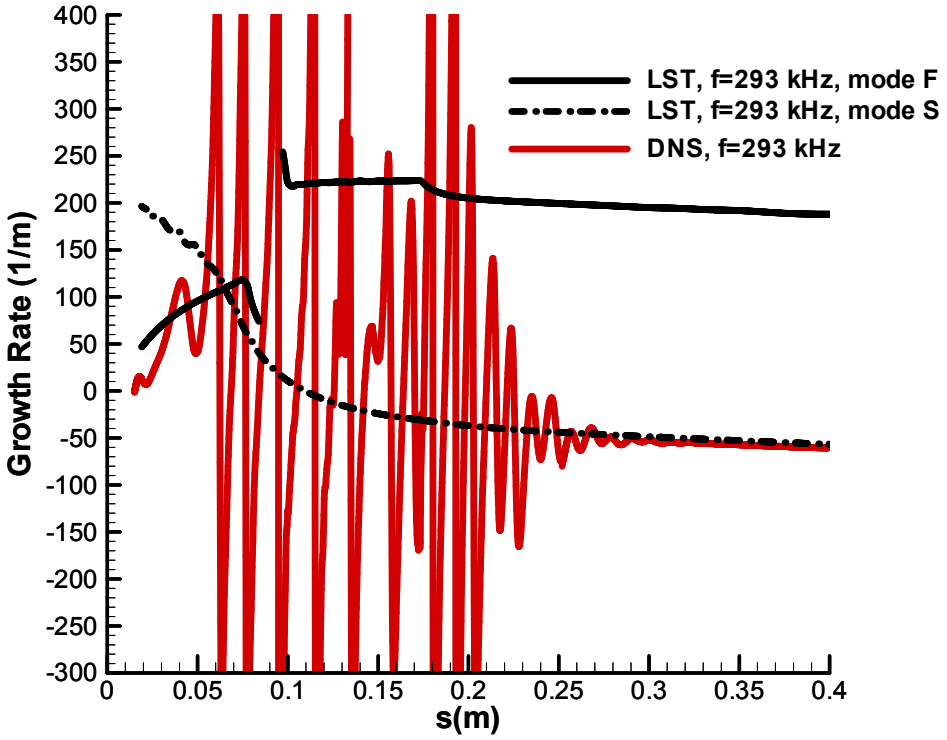

Figure 18. Comparison of negative growth rates of the simulated wall disturbances with those of mode F and S by LST for Case 0.

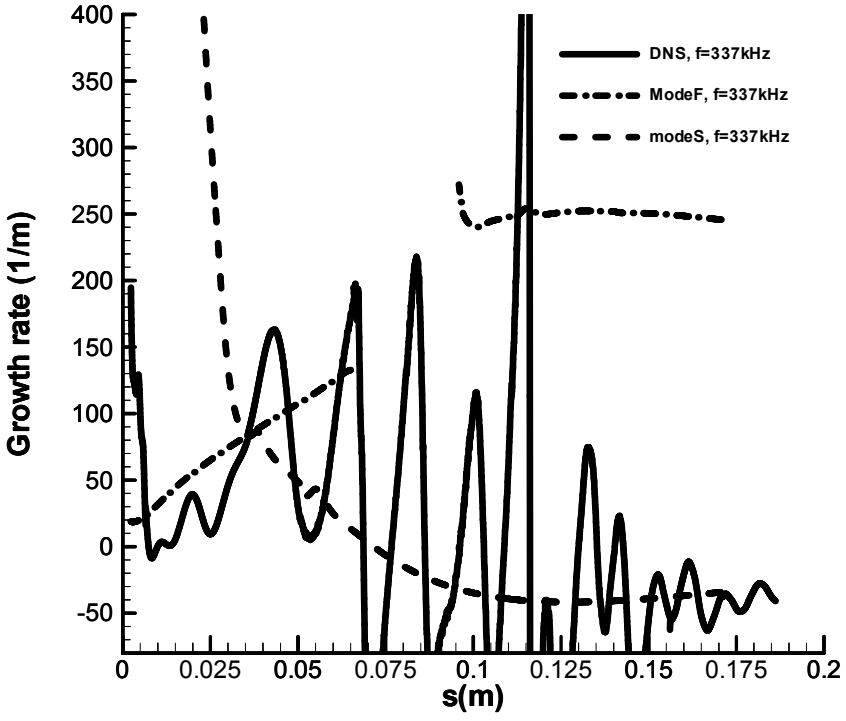

Figure 19. Comparison of negative growth rates of the simulated wall disturbances with those of mode F and S by LST for Case A1.

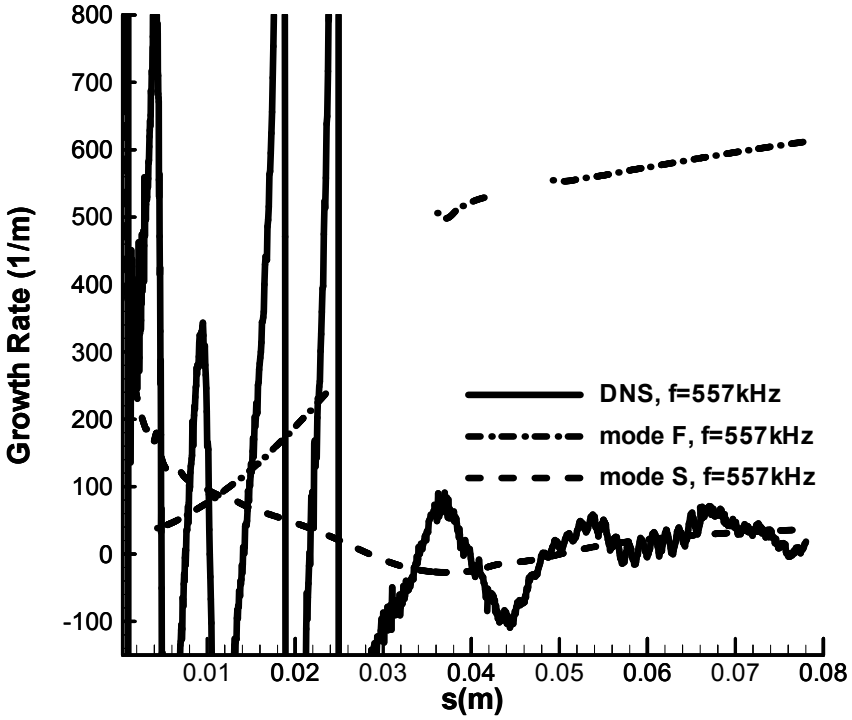

Figure 20. Comparison of negative growth rates of the simulated wall disturbances with those of mode F and S by LST for Case A2.

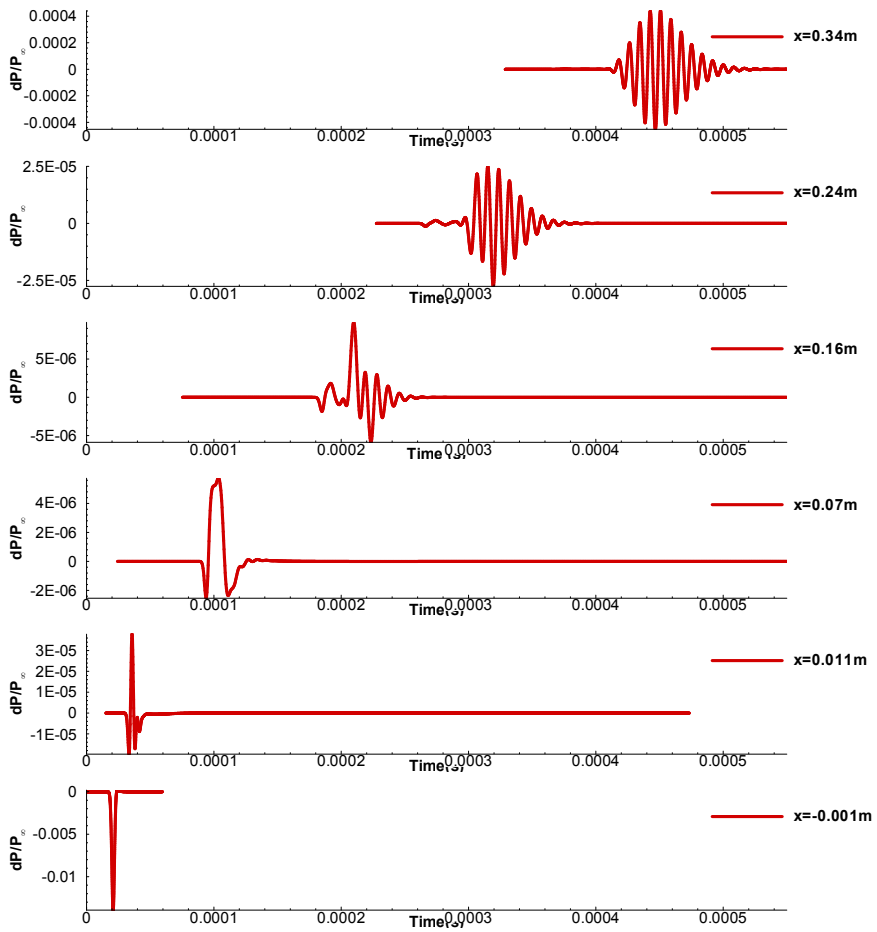

Figure 21. Time-history traces of pressure perturbations at wall at various streamwise locations over the cone for Case B1.

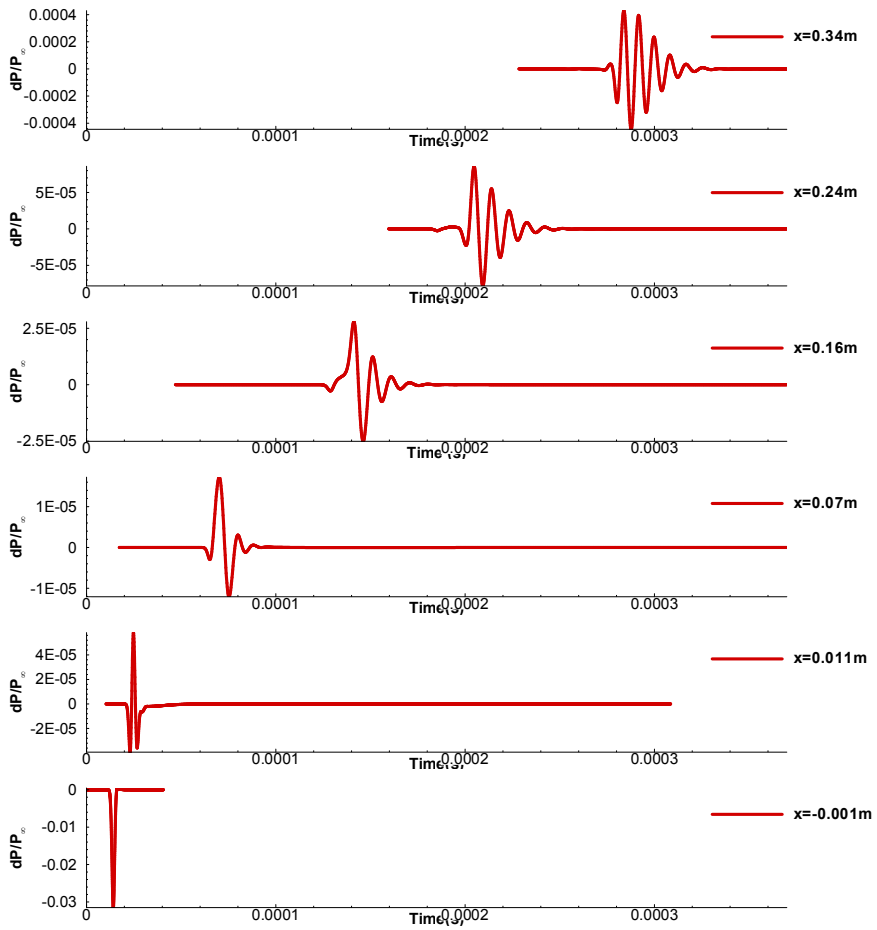

Figure 22. Time-history traces of pressure perturbations at wall at various streamwise locations over the cone for Case B2.

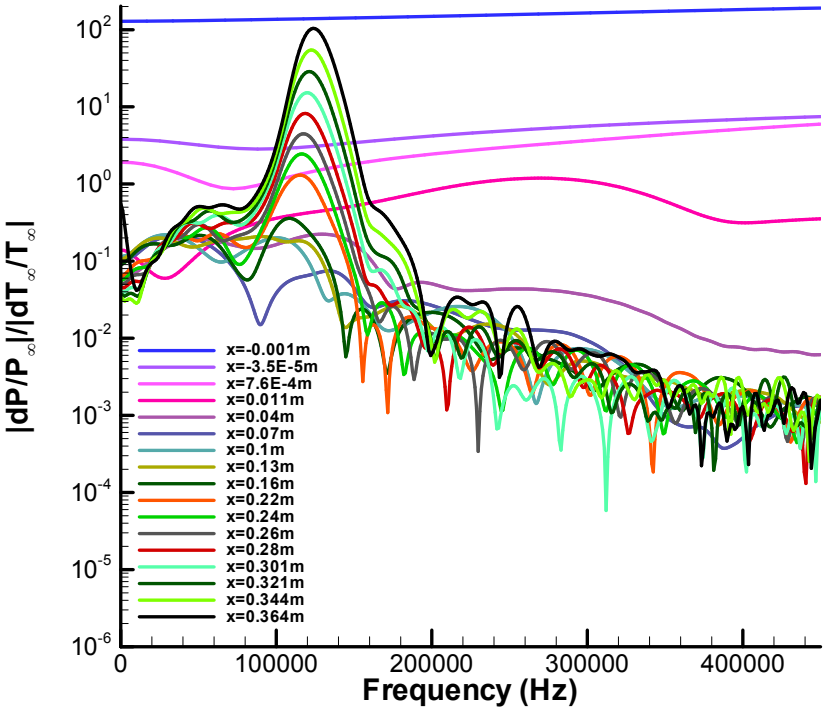

Figure 23. Non-dimensional frequency spectrum of pressure perturbations at wall relative to freestream perturbations at various location over the cone for Case B1.

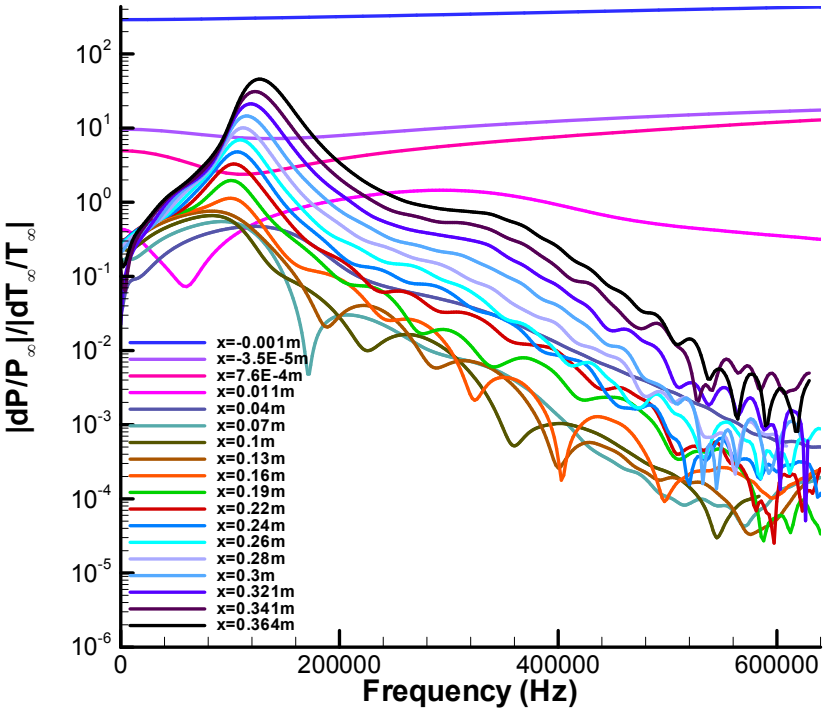

Figure 24. Non-dimensional frequency spectrum of pressure perturbations at wall relative to freestream perturbations at various location over the cone for Case B2.

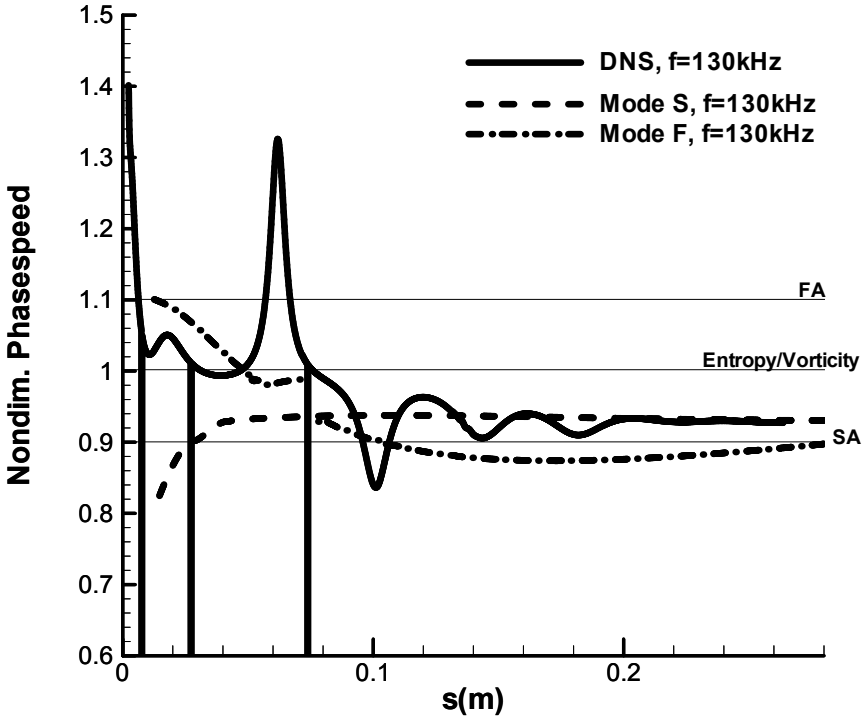

Figure 25. Comparison of the streamwise phase speeds of the simulated wall disturbances with those of mode F and S by LST for Case B1.

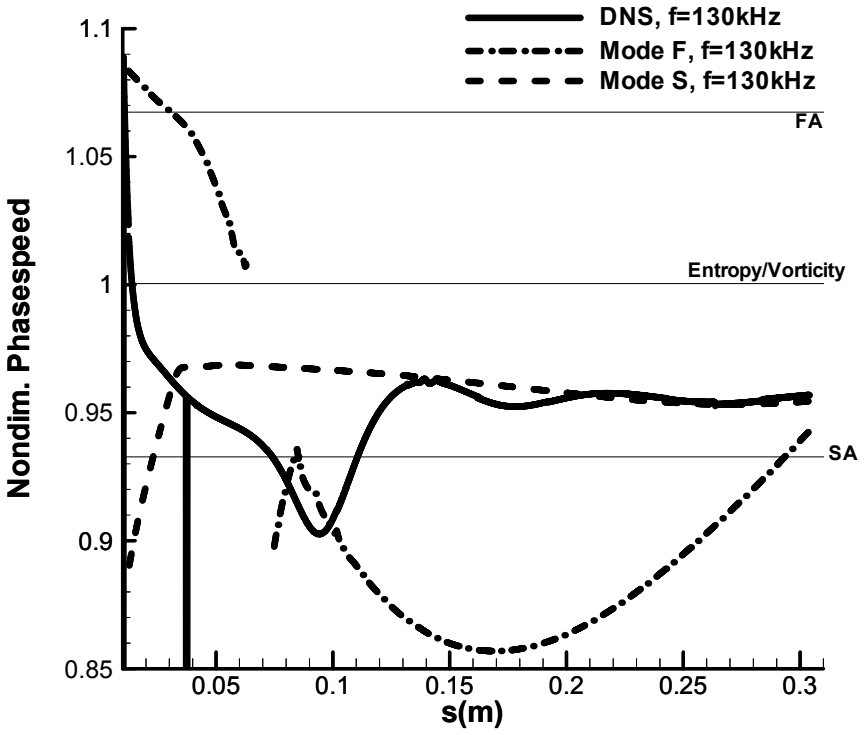

Figure 26. Comparison of the streamwise phase speeds of the simulated wall disturbances with those of mode F and S by LST for Case B2

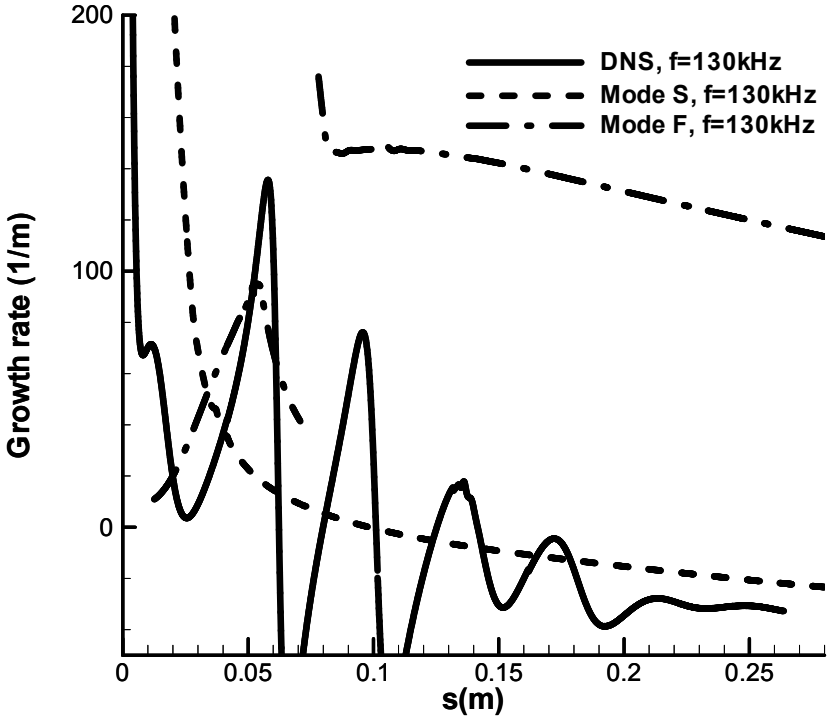

Figure 27. Comparison of negative growth rates of the simulated wall disturbances with those of mode F and S by LST for Case B1.

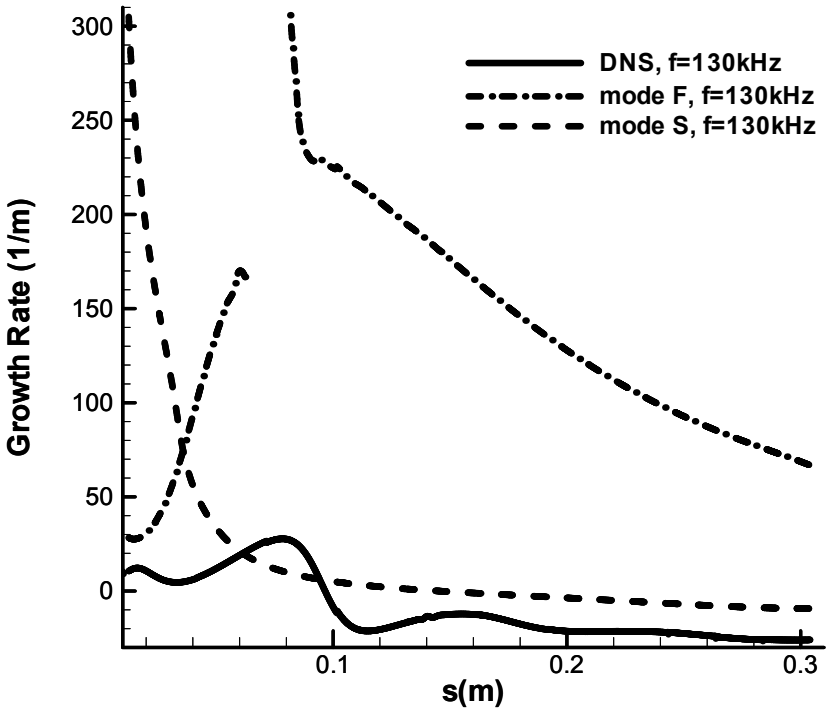

Figure 28. Comparison of negative growth rates of the simulated wall disturbances with those of mode F and S by LST for Case B2.

Acknowledgement

The authors appreciate Professor Steven P. Schneider and his research group at Purdue University for their active collaboration and generous assistance.

References

[1] Dunn, J.W., "Numerical Simulation of Bow-Shock/Disturbance Interactions in Mach-4 Flows Past a Hemisphere" AIAA Paper, 98-0007, January 1998.

[2] Reshotko E., "Hypersonic Stability and Transition", Hypersonic Flows for Reentry Problems, Berlin: Springer, 1991.

[3] Salyer, T.R., "Laser Differential Interferometry for Supersonic Blunt Body Receptivity Experiments", PhD Thesis, Purdue University, May 2002.

[4] Salyer, T.R., Collicott, S.H., Schneider, S.P., "Characterizing Laser-Generated Hot Spots for Receptivity Studies", AIAA Journal, Vol.44, No.12, December 2006.

[5] Schneider, S.P., Wheaton, B.M., Julinao, T.J., Berridge, D.C., Chou, A., Gilbert P.L., Casper. K.M., Steen, L.E., "Instability and Transition Measurements in the Mach-6 Quiet Tunnel", AIAA Paper, 2009-3559, June 2009.

[6] Zhong, X. "High-Order Finite-Difference Schemes for Numerical Simulation of Hypersonic Boundary-Layer Transition", Journal of Computational Physics 144,662-709, April 1998.

[7] Zhong, X., "Receptivity of Mach 6 Flow over a Flared Cone to Freestream Disturbance", AIAA Paper, 2004-253, January 2004.

[8] Zhong, X., Lee, T.K., "Nonequilibrium Real-Gas Effects on Disturbance/Bow Shock Interaction in Hypersonic Flow Past a Cylinder", AIAA, 1996.

[9] Schmisseur, J. D., Collicott, S.H., Schneider, S.P., "Laser-Generated Localized Freestream Perturbations in Supersonic and Hypersonic Flows", AIAA Journal, vol. 38, No.4, April 2000.

[10] McKenzie, J. F., Westphal, K. O., "Interaction of Linear Waves with Oblique Shock Waves", The Physics of Fluids, Vol. 11, No. 11, November 1968.

[11] Kovasznay, L. S. G., "Turbulence in Supersonic Flow", Journal of the Aeronautical Sciences, Vol. 20, No. 10, pp. 657-682, October 1953.

[12] Malik, M. R., "Numerical Method for Hypersonic Boundary Layer Stability", Journal of Computational Physics, 86, 376-413, 1990.

[13] Huang, Y., Zhong, X., "Numerical Study of Laser-Spot Effects on Boundary-Layer Receptivity for Blunt Compression-Cones in Mach-6 Freestream", AIAA paper, 2010-4447, June 2010.

[14] Ward, C.A.C., Wheaton, B.M., Chou, A., Gilbert, P.L., Steen, L.E., Schneider, S.P., "Boundary-Layer Transition Measurements in a Mach-6 Quiet Tunnel", AIAA paper, 2010-4721, June 2010.

[15] Chou, A., "Characterization of Laser-Generated Perturbations and Instability Measurements on a Flared Cone", MS Thesis, Purdue University, December 2010.

[16] Ma, Y., Zhong, X., "Receptivity of a Supersonic Boundary Layer over a Flat Plate. Part 3. Effects of Different Types of Free-stream Disturbances", Journal of Fluid Mechanics, vol. 532, pp. 63-109. December 2004.

[17] Pruett, C.D., Chang, C.L., "Direct Numerical Simulation of Hypersonic Boundary-Layer Flow on a Flared Cone", Theoretical and Computational Fluid Dynamics (1998) 11:49-67, Springer-Verlag 1998.

[18] Balakumar, P., Kegerise, M.A., "Receptivity of Hypersonic Boundary Layers over Straight and Flared Cones", AIAA paper, 2010-1065, January 2010.

[19] Mack, L.M., "Boundary Layer Linear Stability Theory", AGARD report, No. 709, pp.3-1 to 3-81, 1984.

[20] Press et al, "Numerical Recipes The Art of Scientific Computing", Cambridge University Press 1986.

[21] Sivasubramanian, J., Fasel, H.F. "Numerical Investigation of Boundary-layer Transition Initiated by a Wave Packet for a Cone at Mach 6", AIAA paper, 2010-900, January 2010.

[22] Randall, L. A., "Receptivity Experiments on a Hemispherical Nose at Mach 4", M.S. Thesis, School of Aeronautics and Astronautics, Purdue Univ., W. Lafayette, IN, 1996.

[23] Stetson, K.F., Thompson, E.R., Donaldson, J.C., Siler, L.G., "Laminar Boundary Layer Stability Experiments on a Cone at Mach 8, Part 2: Blunt Cone", AIAA paper, 84-0006, January 1984.

[24] Sivasubramanian, J., Mayer, C.S.J., Laible, A.C., Fasel, H.F., "Numerical Investigation of Wavepackets in a Hypersonic Cone Boundary Layer at Mach 6", AIAA paper, 2009-3560, June 2009.

[25] Sivasubramanian, J., Fasel, H. F., "Direct Numerical Simulation of a Turbulent Spot in a Cone Boundary-Layer at Mach 6", AIAA paper, 2010-4599, June 2010.

[26] Sivasubramanian, J., Fasel, H. F., "Transition Initiated by a Localized Disturbance in a Hypersonic Flat-Plate Boundary Layer", AIAA paper, 2011-374, January 2011.

[27] Salyer, T.R., Collicott, S.H., Schneider, S.P., "Feedback Stabilized Laser Differential Interferometry for Supersonic Blunt Body Receptivity Experiments", AIAA paper, 2000-0416, January 2000.

[28] Ladoon, D.W., Schneider, S.P., Schmisseur, J.D., "Physics of Resonance in a Supersonic Forward-Facing-Cavity", Journal of Spacecraft and Rockets, vol. 35, No. 5, September-October 1998.

[29] Chou, A., Wheaton, B.M., Ward, C.A.C., Gilbert, P.L., Steen, L.E., Schneider, S.P., "Instability and Transition Research in a Mach-6 Quiet Tunnel", AIAA paper, 2011-283, January 2011.

[30] Schneider, S.P., Collicott, S.H., "Laminar-Turbulent Transition in High-Speed Compressible Boundary Layers: Continuation of Elliptic-Cone Experiments", Final Report, School of Aeronautical and Astronautical Engineering, Purdue Univ. W. Lafayette, IN, January 2000.

[31] Casper, K.M., Beresh, S.J., Schneider, S.P., "Pressure Fluctuations beneath Turbulent Spots and Instability Wave Packets in a Hypersonic Boundary Layer", AIAA paper, 2011-372, January 2011.

[32] Schmisseur, J.D., "Receptivity of the Boundary Layer on a Mach 4 Elliptic Cone to Laser-Generated Localized Free Stream Perturbations", PhD Thesis, Purdue Univ., W. Lafayette, IN, December 1997.

[33] Heitmann, D., Kahler, C.J., Radespiel, R., "Installation of a System for Laser-Generated Perturbations in Hypersonic Flow", 14th International Symposium on Application of Laser Techniques to Fluid Mechanics, July 2008.

[34] Heitmann, D., Kahler, C.J., Radespiel, R., "Investigation of Laser Generated Perturbations for Boundary Layer Stability Experiments", Numerical & Experimental Fluid Mechanics VII, NNFM 1112, pp. 297-305, Springer-Verlag Berlin Heidelberg 2010.

[35] Heitmann, D., Kahler, C.J., Radespiel, R., Rodiger, T., Knauss, H., Wagner, S., "Non-Intrusive Generation of Instability Waves in a Planar Hypersonic Boundary Layer", Exp Fluids, 50:457-464, Springer-Verlag 2010.

[36] Heitmann, D., Radespiel, R., Kahler, C.J., "Investigation of the Response of a Hypersonic 2D Boundary Layer to Controlled Acoustic Disturbances", AIAA paper, 2010-536, January 2010.

[37] Heitmann, D., Kahler, C.J., Radespiel, R., "Investigation of Laser-Generated Flow Perturbations in Hypersonic Flow over a Flat Plate", AIAA paper, 2008-3737, June 2008.

[38]Huang, Y., Zhong, X., "Numerical Study of Freestream Hot-Spot Perturbation on Boundary-Layer Receptivity for Blunt Compression-Cones in Mach-6 Flow," AIAA paper 2011-3078, June 2011.

[39]Huang, Y., Zhong, X., "Numerical Study of Boundary-Layer Receptivity on Blunt Compression-Cones in Mach-6 Flow with Localized Freestream Hot-Spot Perturbations," NATO AVT-Specialists' Meeting on "Hypersonic Laminar-Turbulent Transition", No. 20, 2012.